MMS Observations of the Multi-Scale Wave Structures and Parallel Electron Heating in the Vicinity of the Southern Exterior Cusp

K. Nykyri [1], X. Ma [1], B. Burkholder [1], R. Rice [1], J. Johnson [2], E-K. Kim [3], P. Delamere [4], A. Michael [5], K. Sorathia [5], D. Lin [6], S. Merkin [5], S. Fuselier [7,8], J. Broll [9], O. Le Contel [10], D. Gershman [11], I. Cohen [5], B. Giles [11], R. J. Strangeway [12], C. T. Russell [12], J. Burch [7]

[1]Department of Physical Sciences and Center for Space and Atmospheric Research (CSAR), Embry-Riddle Aeronautical University, Daytona Beach, Florida, USA
[2]Andrews University, Berrien Springs, MI, USA
[3]Princeton Plasma Physics Laboratory, Princeton, NJ, USA
[4]University of Alaska Fairbanks, Fairbanks, AK, USA
[5]Applied Physics Laboratory, Maryland, MD, USA
[6]NCAR, Colorado, USA
[7]South West Research Institute, San Antonio, TX, USA
[8]University of Texas at San Antonio, San Antonio, TX, USA
[9]University of Boston, Boston, MA, USA
[10]CNRS/Ecole Polytechnique/Sorbonne Université/Univ. Paris-Sud/Obs. de Paris
[11]Goddard Space Flight Center, Greenbelt, MD, USA
[12]University of California, Los Angeles, CA, USA

Key Points:

- MMS observed periodic low frequency waves, likely KHI, at the dawn-flank high-latitude boundary layer.
- Higher frequency waves within the low frequency waves were associated with enhanced Poynting flux and parallel electron heating.
- Waves close to proton cyclotron frequency were identified as Kinetic Alfvén waves, and were evaluated to provide partial heating.

Corresponding author: Katariina Nykyri, `nykyrik@erau.edu`

Abstract

Understanding the physical mechanisms responsible for the cross-scale energy transport and plasma heating from solar wind into the Earth's magnetosphere is of fundamental importance for magnetospheric physics and for understanding these processes in other places in the universe with comparable plasma parameter ranges. This paper presents observations from Magnetosphere Multi-Scale (MMS) mission at the dawn-side high-latitude dayside boundary layer on 25th of February, 2016 between 18:55-20:05 UT. During this interval MMS encountered both inner and outer boundary layer with quasi-periodic low frequency fluctuations in all plasma and field parameters. The frequency analysis and growth rate calculations are consistent with the Kelvin-Helmholtz Instability (KHI). The intervals within low frequency wave structures contained several counter-streaming, low- (0-200 eV) and mid-energy (200 eV-2 keV) electrons in the loss cone and trapped energetic (70-600 keV) electrons in alternate intervals. Wave intervals also showed high energy populations of O^+ ions, likely of ionospheric or ring current origin. The counter-streaming electron intervals were associated with a large-magnitude field-aligned Poynting fluxes. Burst mode data at the large Alfvén velocity gradient revealed a strong correlation between counter streaming electrons, enhanced parallel electron temperatures, strong anti-field aligned wave Poynting fluxes, and wave activity from sub-proton cyclotron frequencies extending to electron cyclotron frequency. Waves were identified as Kinetic Alfvén waves but their contribution to parallel electron heating was not sufficient to explain the > 100 eV electrons, and rapid non-adiabatic heating of the boundary layer as determined by the characteristic heating frequency, derived here for the first time.

1 Introduction

While the solar wind cools as it flows through the solar system, it is rapidly heated when interacting with magnetized planets. The first part of this heating occurs at the planetary bow-shocks, followed by additional heating at the magnetospheric boundary layers, until reaching the highest temperatures inside the planetary magnetospheres. The temperatures in the Earth's dayside central magnetosheath are typically around few 100s of eV for ions and few 10s of eV for the electrons. In-situ spacecraft observations have shown that the Earth's magnetosheath plasma has been significantly heated and rarefied when it penetrates into the magnetosphere, indicating that the heating process is nonadiabatic [*Borovsky and Cayton*, 2011]. Meanwhile, the average temperature ratio between ions and electrons remains nearly the same [*Wing et al.*, 2005; *Wang et al.*, 2012]. This indicates that the non-adiabatic heating (nearly two orders of magnitude) associated with the entry mechanism enhances both the ion and electron temperatures almost by the same proportion.

The main physical mechanisms that transport and heat plasma through magnetic boundaries are magnetic reconnection [*Dungey*, 1961; *Sonnerup and Cahill*, 1967; *Russell and Elphic*, 1978; *Paschmann et al.*, 1979; *Sonnerup et al.*, 1981] and diffusive processes such as transport driven by the kinetic Alfvén waves (KAWs) [*Johnson et al.*, 1997; *Johnson and Cheng*, 2001; *Chaston et al.*, 2007; *Chaston et al.*, 2008]. Also, shear flow driven Kelvin-Helmholtz Instability (KHI) (e.g., [*Fairfield et al.*, 2000; *Otto and Fairfield*, 2000; *Hasegawa et al.*, 2004; *Wing et al.*, 2014; *Masson and Nykyri*, 2018]) can lead to plasma transport and heating via secondary processes such as magnetic reconnection [*Otto and Nykyri*, 2003; *Nykyri et al.*, 2017; *Ma et al.*, 2017] and turbulent mixing through thin boundaries created by the KHI [*Thomas and Winske*, 1993; *Fujimoto and Terasawa*, 1994; *Wilber and Winglee*, 1995; *Matsumoto and Hoshino*, 2004; *Nakamura et al.*, 2011; *Cowee et al.*, 2009; *Delamere et al.*, 2011].

Recently, it has been demonstrated using Hall-magnetohydrodynamics (MHD) with test particles and hybrid simulations that plasma is mainly transported through a few big magnetic islands caused by KHI-driven reconnection in the fluid simulation, while hybrid simulation produces small and patchy magnetic islands [*Ma et al.*, 2019]. These simulations also revealed that KHI, in its non-linear stage, can lead to anisotropic (perpendicular vs. parallel) temperature ratios in the different regions of the vortex structures which may lead to wave-excitation. The temperature asymmetries can also be created by magnetic reconnection: *Hietala et al.* [2015] showed how the boundaries of reconnection exhaust originating from magnetotail reconnection had larger parallel ion temperatures ($T_{i\parallel} > T_{i\perp}$). Also, the reconnection jet driven magnetic flux pileup can generate anisotropic electron distributions with perpendicular electron temperature anisotropy ($T_{e\perp} > T_{e\parallel}$) that can drive parallel propagating whistler waves [*Le Contel et al.*, 2009; *Khotyaintsev et al.*, 2011]. The prevailing solar wind conditions and Interplanetary Magnetic Field (IMF) orientation determines the properties of the magnetosheath plasma and the relative importance of these physical mechanisms. For southward IMF magnetic reconnection in the vicinity of the dayside magnetopause dominates the mass and energy loading of the magnetosphere (see e.g, *Burch et al.* [2016] and reference therein), whereas for northward IMF the double high-latitude reconnection tailward of the cusps [*Song and Russell*, 1992; *Li et al.*, 2005; *Fuselier et al.*, 2019] and the KHI [*Nykyri and Otto*, 2001; *Taylor et al.*, 2008; *Ma et al.*, 2017; *Sorathia et al.*, 2019] become dominant processes responsible for mass loading of the magnetosphere. As the strongly northward and southward IMF conditions are relatively rare [*Dimmock et al.*, 2013], the IMF y-and x component play a crucial role on the location of the shock geometry and draping conditions at the magnetopause downstream from the shock [*Nykyri*, 2013] which can lead to dawn-dusk asymmetries of the low latitude and high-latitude reconnection and KHI, and result in asymmetric heating.

The MMS spacecraft recorded the first, detailed measurements of reconnection exhausts associated with the strongly compressed current sheets created by the Kelvin-Helmholtz (KH) waves during northward IMF [*Eriksson et al.*, 2016; *Li et al.*, 2016]. This same KH event also contained large-amplitude, parallel, electrostatic waves [*Wilder et al.*, 2016]. The reconnection process is closely associated with the development of kinetic-scale fluctuations *[Drake et al., 1994; Vetoulis and Drake, 1999; Chaston et al., 2005, 2009; Gershman et al., 2017]*. Whistler modes and kinetic Alfvén waves can be produced by current driven instabilities and may play a role in magnetic reconnection and plasma transport *[Chaston et al., 2009]*. Since diffusion regions are tiny, not much plasma can be circulated through it. The scale analysis based on the pressure balance shows that magnetic reconnection alone under the typical magnetopause environment is not able to provide a sufficient macroscopic non-adiabatic heating source [*Ma and Otto*, 2014]. The heating mechanism needs to have a volume filling effect in order to explain the observed level of magnetospheric specific entropy increase. A significant volume of the Earth's magnetosphere is adjacent to the velocity shear layer created by the shocked solar wind flow along the magnetopause. As the typical velocity shear layer thickness is about one to two orders of magnitude larger than the ion inertial length (40-100 km for proton number densities of 40/cc and 10/cc, respectively) at the vicinity of the dayside magnetopause [*Sckopke et al.*, 1981; *Nykyri and Dimmock*, 2016], the energy conversion from solar wind bulk flow kinetic energy into the thermal energy of the magnetospheric particles must be through a "cross the scale" fashion spanning MHD, ion and electron scales.

Clues to a heating source may be provided by examining the origin of the dawn-dusk asymmetries of the heated plasma. The upstream shock geometry can lead to dawn-dusk asymmetries of several magnetosheath plasma quantities (see e.g., *Walsh et al.* [2014] and *Dimmock et al.* [2017] and references therein), which can contribute to the magnetospheric asymmetries. For example, the heating and transport of the cold component ions favors the dawn-sector [*Hasegawa et al.*, 2003; *Wing et al.*, 2005]. A statistical study of magnetosheath temperatures has revealed that ion magnetosheath temperatures downstream of quasi-parallel (dawn-flank for Parker-Spiral IMF) bow shock are only up to 15 percent higher than downstream of the quasi-perpendicular shock [*Dimmock et al.*, 2015] which is not adequate to explain the 30-40% asymmetry in the plasma sheet [*Wing et al.*, 2005]. Spatial distribution of the KH waves observed between 2007-2013 has revealed a dawn flank-favored asymmetry during mainly the Parker-Spiral (PS) IMF orientation while for strongly northward IMF more events were observed at the dusk but favored higher solar wind speed [*Henry et al.*, 2017], due to increased magnetic tension at the dusk flank due to draped PS horizontal component. The KH waves at the dawn-flank magnetopause are shown to be associated with the enhanced ion-scale magnetosonic and kinetic Alfvén wave-activity with adequate Poynting flux to explain the observed level of ion heating [*Moore et al.*, 2016, 2017]. Ion beams generated by the reconnection in KH vortices *[Nykyri et al., 2006]* could also drive electromagnetic wave activity at ion scales. Also, turbulent processes associated with the KHI [*Stawarz et al.*, 2016] can contribute to the plasma heating [*Kaminker et al.*, 2017; *Burkholder et al.*, 2020b]. For northward IMF, *Sorathia et al.* [2019] showed, using a combination of global MHD and test-particle simulations, that cusp particle entry further contributes to the dawn-dusk temperature asymmetry due to asymmetric particle heating in the cusp.

In general, the role of the physical processes is to reduce the sources of free energy. These free-energy sources can be provided for example by the velocity shear and magnetic shear. There are several processes that allow cross-scale energy transport from fluid-scale Kelvin-Helmholtz (KH) waves into ion and electron scales that could operate both at low and high-latitudes. To summarize, we list below the following five mechanisms that we are aware of (but there may be others):

Mechanism 1A): Secondary reconnection close to the plane of the velocity shear [*Nykyri and Otto*, 2001, 2004; *Nykyri et al.*, 2006; *Eriksson et al.*, 2016; *Li et al.*, 2016]. The in-plane reconnection such as observed by *Nykyri et al.* [2006] was associated with ion beams. It is well known that the ion beams can drive various ion-scale wave activity (e.g., ion cyclotron waves) which can resonantly interact with ions. The KH waves have been associated with enhanced ion cyclotron-range wave activity when compared to boundary crossings without active KH wave activity [*Moore et al.*, 2017].

Mechanism 1B): Secondary KHI driven "Mid-latitude", reconnection [*Ma et al.*, 2017]. This can result in the development of the shell-like ion distribution functions [*Nykyri et al.*, 2020]. These shell distributions have free energy to drive kinetic magnetosonic waves that were previously shown to explain the observed level of ion heating at the flank magnetopause [*Moore et al.*, 2016].

Mechanism 2) Ultra-low frequency waves (below 0.5 Hz) can be associated with mode conversion [*Lee et al.*, 1994; *Belmont et al.*, 1995; *De Keyser et al.*, 1999] which can explain the amplification of the perpendicular wave power at the magnetopause: compressional MHD waves can mode convert into Kinetic Alfvén Waves (KAWs) at the magnetopause [*Johnson et al.*, 2001]. These KAWs have been expected to be strong contributors for plasma heating and mixing in Low Latitude Boundary Layer (LLBL) [*Johnson et al.*, 1997; *Johnson and Cheng*, 2001]. *Chaston et al.* [2007] showed observations of large Alfvén speed gradients at the LLBL generated by the KHI. The results were consistent with the mode conversion from surface waves to KAWs and transport of both electromagnetic energy and plasma at the Alfvén resonance.

Mechanism 3) Possible generation of other plasma wave modes due to inhomogeneities and sharp gradients generated by the KHI, for example generation of perpendicular vs parallel temperature asymmetry [*Ma et al.*, 2019] that can lead to kinetic wave excitation.

Mechanism 4) Turbulent cascade and turbulent heating from MHD scales to ion and electron scales [*Stawarz et al.*, 2016; *Burkholder et al.*, 2020b; *Hasegawa et al.*, 2020].

It is important to understand the effectiveness and relative contribution of the different physical mechanisms on the ion and electron heating under different solar wind and magnetosheath/magnetopause conditions. The present paper is motivated by simultaneous MMS observations of the multi-scale plasma wave structures (spanning fluid, ion and electron frequency scales) and parallel heated electrons at the dawn-sector high-latitude dayside magnetosphere during northward, ortho-Parker Spiral IMF orientation. Therefore, our first step was to identify these different plasma wave modes. Once the wave modes and properties are identified their efficiency for plasma heating can be evaluated in combination with plasma physics theory. However, due to Doppler shifts, identifying a plasma wave mode unambiguously in terms of experimental dispersion relation is possible only if two or more spacecraft see the same wave structure. Therefore, we selected this event for further study as the burst mode search coil magnetometer (SCM) data revealed an interval where at least two MMS spacecraft identified the same wave packet at the strong gradient of Alfvén velocity where strong Ohmic heating was observed.

As magnetosheath flow is nearly perpendicular to magnetospheric field lines and based on the growth rate calculations, we demonstrate that KHI can be generated in this region for the prevailing IMF and magnetosheath conditions. KHI has also been previously observed in the northern hemispheric high-latitude boundary layer [*Hwang et al.*, 2012; *Ma et al.*, 2016]. The observed low frequency wave structures are associated with high-frequency plasma waves and enhancements of the parallel electron temperature as well as trapped high energy electrons during some intervals. The kinetic scale plasma waves, with largest amplitudes and corresponding to the strongest anti-field-aligned Poynting flux and counter-streaming electrons, were identified as KAWs. We show that for the identified interval, the KAWs are not solely responsible for rapid heating of the boundary layer.

The paper is organized as follows. Section 2 discusses the data and instruments used in the study. Section 3 discusses 1) Overview observations of the event, 2) Scatter Plot Characterization of Boundary Layer Plasma and Various Instability Criteria, 3) Minimum Variance Analysis of Low Frequency Fluctuations and Field Aligned Poynting Flux at the Outer Boundary Layer, 4) Burst Mode Analysis of Field Aligned Poynting Flux, Electron Heating and Plasma Wave Characteristics, and 5) Plasma Wave Mode Identification Using Two-spacecraft Method. Section 4 concludes and discusses the research findings.

2 Methodology

2.1 Data and Instrumentation

All magnetospheric data shown in Figures 2-10 are the level 2 data from NASA's MMS satellites [*Burch et al.*, 2016]. We use Hot Plasma Composition Analyzer (HPCA) for the H+, He++, and O+ ion phase space-energy spectrograms [*Young et al.*, 2016]; Fast Plasma Investigation (FPI) [*Pollock et al.*, 2016] for the ion and electron energy spectra and moments; Flux Gate Magnetometers (FGM) [*Russell et al.*, 2016; *Torbert et al.*, 2016] for the DC magnetic field and Search Coil Magnetometers (SCM) for the AC magnetic field [*Le Contel et al.*, 2016; *Torbert et al.*, 2016]. Energetic ion and electron distribution and pitch angle (PA) data comes from the Fly's Eye Energetic Particle Spectrometer (FEEPS) [*Blake et al.*, 2016] instrument. The Electric field is from spin-plane and axial Double Probes (EDP) [*Lindqvist et al.*, 2016; *Ergun et al.*, 2016; *Torbert et al.*, 2016]. The versions of the data files used are v4.22.0 for FGM (survey mode cadence of 16 Hz); v4.25.0 for FGM (burst mode cadence of 128 Hz); v2.2.0 for SCM (burst mode cadence of 8192 Hz), v2.1.0 for EDP (fast mode cadence of 32 Hz); v2.2.0 for EDP (burst mode cadence of 8192 Hz); v3.3.0 for FPI (burst mode cadence of 150 ms for ions and 30 ms for electrons, respectively, and the fast mode cadence of 4.5 s); v4.1.0 for HPCA (survey mode cadence of 10 s); v6.0.2 for FEEPS (survey mode cadence of 19.4 s); v6.0.3 for FEEPS (burst mode cadence of 0.3 s), respectively. Solar wind conditions are taken from the OMNI (http://omniweb.gsfc.nasa.gov/) database [*King and Papitashvili*, 2005]. Figure captions indicate when burst mode data is used.

In the present paper we are focusing on the electromagnetic wave analysis using FGM, SCM and EDP and for plasma regime (< 30 keV) using the FPI instrument. We are only including the 70-600 keV energetic particle observations from FEEPS as well as the ion composition from HPCA for context.

3 MMS Observations

3.1 Overview of the Observations

Figure 1 shows MMS location with respect to Earth's magnetosphere on 25th of February, 2016 between 19:00-20:00 UT during the event interval and Figure 2 presents an overview plot (see caption for more details) of the MMS 3 observations in GSM coordinates between 18:55-20:05 UT at the dawn sector ($y \approx$ -10 R_E), high-latitude ($z \approx$ -6 R_E) dayside ($x \approx 1$ R_E) magnetopause. Due to small spacecraft separation of ≈ 30 km, all the MMS spacecraft observe essentially the same large scale plasma and field properties. The IMF is northward and the horizontal component is in the Ortho-Parker Spiral orientation, ($B_{IMF} \approx$ [-8, -5, +4] nT in GSM-coordinates).

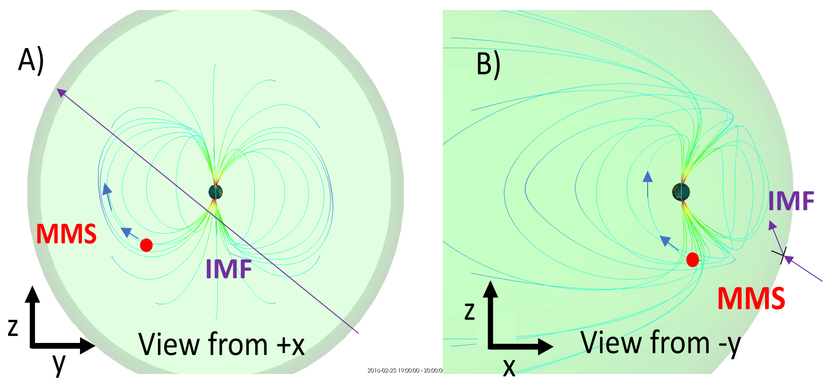

Figure 1. Three−dimensional visualization of the Earth's magnetic field topology computed using T96 model [*Tsyganenko*, 1996] and the MMS location between 19:00-20:00 UT on the 25th of February 2016 in z, y (a) and x, z (b) planes (in GSM coordinates), respectively. The magnetic field direction is shown with blue arrows. The IMF (purple arrow) is northward and becomes more northward at the dayside magnetosheath due to shock deflection. The horizontal component of IMF is in the Ortho-Parker Spiral orientation, ($B_{IMF} \approx$ [-8, -5, +4] nT in GSM-coordinates).

Up to ≈ 19:32 MMS travels at the inner boundary layer (closer to magnetosphere) characterized by quasi-periodic variations between higher energy magnetospheric ions (> 2-3 keV) and electrons (> 500 eV) and lower energy (≈ 20 eV to 2 keV) magnetosheath ions (panel 2) and (≈ 10 eV to 200 eV) electrons (panel 4). In the inner boundary layer there are higher fluxes of higher energy particles and the low energy component is at the higher energy than in the outer boundary layer between 19:32-19:57. In the inner boundary layer there also exists more energized double ionized helium, He^{++}, than at the outer boundary layer, while the fluxes of the lower energy He^{++} from solar wind origin increase in the outer boundary layer (panel 5). The energetic component of O^+ is more continuous at the inner boundary layer and becomes more patchy at the outer boundary layer (panel 6). The high energy O^+ could either originate from the ring current or be of ionospheric origin that has been energized in the high-latitude diamagnetic cavities [*Nykyri et al.*, 2012; *Nykyri et al.*, 2019a]. High energy ions and electrons (panels 1 and 3) persist throughout the interval, with the trapped electrons (panel 14) being more abundant in the inner boundary layer. In the inner boundary layer the plasma density is lower and temperature higher (panel 7) and the tailward component (v_x) of the plasma flow velocity is small (panel 8). From about 19:50 to 20:00 the spacecraft alternate between the outer boundary layer and the magnetosheath. In the magnetosheath, the tailward plasma velocity and density increase and the temperature decreases. Ion beta (panel 9) varies between 0.1-1.2 and T_i/T_e (panel 10), which is typically quite well conserved during plasma entry [*Wang et al.*, 2012] varies between 3 to 28 and reaches smaller values at the outer boundary layer.

Throughout the interval, the magnetic pressure dominates over the plasma pressure of the low energy species (panel 11). The mostly negative B_x and B_y, and positive B_z (panel 12) are consistent with the expected magnetic field topology (see Figure 1a and b), as the outward diverging magnetic field originating from the southern hemispheric cusp should have a negative B_x and B_y, and positive B_z at the southern hemispheric, high-latitude dawn-sector boundary layer. At the outer boundary layer at 19:40-19:57 magnetic field B_x and B_z components show periodic wave structures with rapid leading edge and more gradual trailing edge (see this more clearly in Figure 4). Note that the solar wind plasma number density is high ($\approx$ 16-23/cc) at 19:00-20:05 UT making the magnetosheath density higher than typical. The high energy (70-600 keV) ions at the inner boundary layer between 19:02 -19:15 are mostly in the loss cone (panel 13) while during the local magnetic field depressions there also appears a trapped population. High energy electrons (70-600 keV) (panel 3 and 14) are mostly trapped throughout the interval with the highest fluxes also typically coinciding with the local magnetic field depressions (panel 16). The local loss cone pitch angle, α, calculation assumes adiabatic electron motion and uses similar methods as in the previous studies (see e.g., *Nykyri et al.* [2012]; *Lavraud et al.* [2016]; *Nykyri et al.* [2019a]):

$$\alpha = \arctan\left(\frac{1}{\sqrt{B_M/B - 1}}\right), \tag{1}$$

where a constant magnetic field value, B_M = 55 nT at the mirror point is used (which is also the maximum magnetic field observed by MMS during this interval) and B is the local magnetic field magnitude observed at each given point between 18:55-20:05 UT.

Low energy (0-200 eV) electrons (panel 15) both at the inner and outer boundary layer are mostly in the loss cone and show a counter-streaming-structure.

3.2 Scatter Plot Characterization of Boundary Layer Plasma and Various Instability Criteria

Figure 3 shows data from all four MMS spacecraft organized in a scatter plot-format using FPI moments and magnetic field (interpolated into same time tags) between 18:55-20:05 UT. Figure 3a shows plasma number density for ions versus v_x-component of the ion velocity, where each point is color coded and sorted with ion specific entropy, $S_i = T_i/n_i^{2/3}$, respectively. Figure 3b shows the same for the corresponding electron moments. Clear magnetospheric, magnetosheath, and tailward-accelerated (twa) and heated boundary layer (BL) populations are marked with rectangles. The rest of the points have plasma characteristics of a typical boundary layer plasma. Similar to *Hasegawa et al.* [2006], this shows a portion of the lower density ($2/cc < n < 4/cc$), heated ($S > 20$ eV$/cm^2$) boundary layer electron plasma to move faster (v_{ex} < -220 km/s) than the typical sheath flow (v_{ex} < -150 km/s). The "faster than sheath" BL plasma has typically been interpreted as a signature of rolled up Kelvin-Helmholtz vortex: due to conservation of the angular momentum, low density plasma inside vortex moves faster than the higher density sheath plasma. Please note that for the ions the heated boundary layer plasma does not reach such high velocities as for the electrons, which may be explained by the larger ion gyroradius compared to the width of the narrow acceleration region within the vortex. The high density sheath plasma has lower specific entropy (black symbols) than the magnetospheric plasma with low velocity (red symbols). Note that the low density, faster than the typical sheath flow population has higher specific entropy than the sheath plasma. However, the signature of the faster than sheath plasma is not unique to rolled-up KH vortices. For northward IMF and significantly sunward of the terminator the surface waves with presence of plasma depletion layer can also show this feature [*Plaschke et al.*, 2014]. The present event occurs very close to dawn-dusk terminator, at higher latitudes and for different IMF orientation (with $|B_x| > |B_y| > |B_z|$) so the present observations can't be directly compared with those by *Plaschke et al.* [2014].

Figure 3c presents specific entropy for the electrons (normalized to minimum electron entropy) vs electron velocity where the maximum electron velocity for the interval has been extracted, so that the zero velocity corresponds to sunward flowing plasma. Color code is the total pressure (including magnetic field pressure and electron and ion plasma pressures). Kelvin-Helmholtz vortex center should be characterized by a total pressure minimum (see e.g., *Otto and Fairfield* [2000]; *Nykyri et al.* [2006]; *Nykyri and Foullon* [2013]). The bottom right portion of the plot shows high entropy, high tail-ward velocity plasma characterized by low total pressure (darker blue and purple asterisks), so this is consistent with MMS spacecraft encountering plasma close to the vortex center during the interval. Figure 3d shows ion temperature anisotropy ($T_\perp/T_\parallel$) vs parallel ion beta, $\beta_\parallel = 2\mu_0 n k T_\parallel / B^2$, color coded and sorted by ion specific entropy. The threshold criteria for mirror mode, proton cyclotron, fluid fire hose, parallel firehose and oblique fire hose instabilities are plotted after equations from [*Hellinger et al.*, 2006]. It can be seen that a portion of the boundary layer plasma satisfies the criteria for the proton cyclotron instability. Figure 3e shows the same quantities for the electrons with the curves highlighting the threshold for the whistler and electron fire hose instability. None of the data points satisfy these instability thresholds.

In order to evaluate the time scale of the non-adiabatic plasma heating during the present event, we use here the equation for the characteristic heating frequency, f_{heat} (see Appendix for the derivation of this equation).

$$f_{heat} = \frac{1}{S}\frac{dS}{dt} = \frac{\eta J^2}{P/(\gamma-1)}. \tag{2}$$

The right hand side of the equation 2 is the Ohmic heating (ηJ^2) to plasma thermal energy density ($P/(\gamma-1)$) ratio. The anomalous Ohmic heating" term can computed from the perspective of the Hall-MHD by taking the dot product of the Hall-MHD Ohm's law (see e.g., [*Nykyri*, 2002; *Nykyri and Otto*, 2004]) as:

$$(\mathbf{E} + \mathbf{v_e} \times \mathbf{B}) \cdot \mathbf{J} = \eta J^2, \tag{3}$$

where the electric field, magnetic field and current (from curlometer) are interpolated into the same time tags as the FPI instrument fast sampling rate electron velocity. Please note that in the generalized Ohm's law, there are electron pressure gradient terms and electron inertial terms, which can break the frozen-in condition and contribute to the heating or cooling. Therefore, this "anomalous heating" can be negative. Here, we only care about the time-scale of heating or cooling and therefore have taken an absolute value of the "anomalous Ohmic heating term". The plasma energy density is computed from the $P/(\gamma-1)$, where γ is the ratio of the specific heats, 5/3. All quantities are interpolated to the center of the MMS tetrahedron.

Figure 3f shows the ion to electron temperature ratio vs normalized electron entropy, and each data point is color coded and sorted based on the "Characteristic heating frequency" calculated from the entropy equation (see equations 2 and 3) where the "anomalous Ohmic heating" is divided by the "plasma thermal energy density". It is apparent that the ion to electron temperature ratio is not constant but ranges from values of ≈ 3-7 in the low electron entropy magnetosheath (see also panel b) where the low entropy plasma is in the magnetosheath) to the highest values above 25 in the mid-entropy region, and above 10 in the highest entropy region. The concentration of points with most rapid heating (red-orange dots) occurs in the low entropy magnetosheath, where the ion to electron temperature ratio is low (4-7), but the rapid heating continues with somewhat steadily increasing ion to electron temperature ratio to the higher electron entropy magnetosphere. The median "Heating frequency" is 21 Hz which suggests extremely rapid heating of the boundary layer by the electro-magnetic fields.

3.3 Minimum Variance Analysis of Low Frequency Fluctuations and Field Aligned Poynting Flux at the Outer Boundary Layer

Figure 4 shows 25 minutes of MMS 3 observations between 19:40-20:05 of the outer boundary layer in the similar format as in the KHI event with kinetic Alfvén waves observed by Cluster [*Chaston et al.*, 2007]. Panels from top to bottom present magnetic field (a), magnetic field rotated into 90 s sliding window minimum variance of magnetic field (MVAB) coordinates [*Sonnerup et al.*, 1995] (b), electric field (c), electric field rotated into MVAB coordinates (d) same as in panel b, low energy ion (e) and electron (f) spectrograms, low energy (0-200 eV) electron pitch angle distribution (g), Alfvén speed (h), and the Poynting flux, $\mathbf{S} = \mathbf{E} \times \mathbf{B}/\mu_0$, which is rotated along the minimum variance direction which is computed using 90 second sliding window (i), and the angles between 90 s minimum variance direction and average boundary normal (j). The average boundary normal, computed using MVAB on 25 minutes of data, is $n = [0.41, -0.91, 0.03]$ in GSM coordinates and the 90 s sliding window is applied to the individual MVAB calculations with 20 s shift. The subscripts i, j and k stand for the maximum, intermediate and minimum variance directions, respectively. The Alfvén speed is computed using ion densities from FPI. The mass density correction to the Alfvén speed calculation from heavier ions can be evaluated from the relative abundances of H+, O+ and He++ (from HPCA) and would be ≈ 5 percent, and is not included in this calculation.

The quasi-periodic low frequency wave-like signature is clear in z and x -components of the magnetic field (a) and becomes more pronounced in the maximum (B_i) and intermediate (B_j) variance components of the magnetic field (b). The wave structure is also apparent in quasi-periodic variation of the angle between individual minimum variance direction and average boundary normal. A more suitable coordinate system for studying boundary normal variations due to KHI is presented in *Ma et al.* [2016], here we choose to use MVAB to decompose the low frequency oscillations into parallel (k) and to perpendicular (i, j) components to characterize the fluctuation frequencies perpendicular to background field. During this 25 minute interval there are roughly 16 and 11 clear peaks in the B_i and B_j, corresponding roughly periods of 94 s and 136 s, respectively.

Maximum fluxes of counter-streaming low energy electrons (g) are seen at the local minima of the Alfvén speed which correspond to heated, magnetosheath-like plasma with the typical lower energy ion (e) and electron (f) populations. The positive peaks of the Poynting flux rotated into minimum variance direction (i) typically match the 180 and 0 degree electron populations (depicted with orange columns) whereas the strongest troughs (strong negative S_k) in the Poynting flux correlate with higher Alfvén speed (magnetospheric like plasma) and lower fluxes of low-energy electrons (depicted with purple columns). The purple column with red arrow highlights an interval of a strong, 350 $\mu W/m^2$ anti-field aligned (Earthward) Poynting flux close to Alfvén speed gradient. This highlighted interval will be studied in the following sections in more detail.

Figure 5 shows power spectral density (computed using a Fast Fourier Transform) of the B_i (a) and B_j (b) fluctuations confirming roughly the frequencies from the visual inspection. Maximum power of 19.7 nT^2/s in B_i fluctuations corresponds to the frequency of 0.01 Hz and adjacent to the maximum power peak there is a lower, not well separated peak at 0.013 Hz. These frequencies correspond to the periods of 75 s and 100 s. For B_j the maximum power of 25.5 nT^2 corresponds to frequency of 0.002 Hz (period of 500 seconds), and the 2nd peak at 16.9 nT^2/s corresponds to frequency of 0.007 Hz (period of 136 seconds). For B_j there exists a well separated 3rd peak at 0.01 Hz, however with less power (2.5 nT^2/s) than the corresponding peak in B_i.

Solar wind and IMF data (determined from visual inspection from 15 s Wind spacecraft magnetic field and 60 s resolution plasma data) do not show peaks in the vicinity of 0.01 Hz. However, there are significant solar wind dynamic pressure variations on a time scale comparable to the 500 s low frequency fluctuations so it is likely that they may be expected to drive some of the variability observed by the MMS in the vicinity of the southern cusp.

For the KH instability, the fastest growing wave mode should have a frequency of $f = v_{ph}/\lambda$, where λ is the wave length and v_{ph} is the phase speed. The fastest growing wave mode should be proportional to the boundary layer thickness, Δ, such that $k\Delta = 0.5$-1, where k is the wave number [*Miura and Pritchett*, 1982]. This corresponds to a wave length of $\lambda = 2\pi\Delta - 4\pi\Delta$. The KH wave phase velocity can be estimated from

$$\mathbf{v}_{\mathrm{ph}} = \frac{n_1\mathbf{v}_1 + n_2\mathbf{v}_2}{n_1 + n_2} = 107.18 km/s\hat{\mathbf{k}} \tag{4}$$

Here subscripts 1 and 2 refer to observed magnetosheath and magnetospheric values shown in Table 1, respectively, with n_1 = 39.5/cc, n_2 = 3.2/cc, $\mathbf{v}_1$ = 115.38 km/s, and $\mathbf{v}_2$ = 5.66 km/s, where $\mathbf{v}$ on either side is projected along the KH wave k-vector direction (which is computed below). Using a typically observed dawn sector magnetopause thickness of 1410 km [*Haaland et al.*, 2019], the fastest growing KH wave mode should have a wave length of $\lambda_{KH} = (2-4)\pi\Delta$ = 1.4-2.8 R_E, and an upper frequency limit approximately in the range of $f = \frac{v_{ph}}{\lambda_{KH}}$ =0.006-0.012 Hz, which is in good agreement with the observed frequencies. However, the velocity boundary layer thickness at the dawn-sector in the vicinity of the high-altitude cusps is likely much larger than the above estimate of 1410 km of the magnetopause thickness [*Sckopke et al.*, 1981; *Nykyri and Dimmock*, 2016], and depends also on the previous reconnection history, topology and orientation of the subsequent Earthward flow channels in the vicinity of the exterior cusp. Using an upper estimate of the velocity shear layer thickness of 1 R_E would give the low frequency limit for the fastest growing KH mode of 1.3-2.7 mHz. If the IMF orientation is changing within KH growth time and results in differently orientated earthward flow-channels, it may be possible to generate a spectrum of KH waves with different propagation angles, wave lengths and phase speeds leading to wave-wave interference [*Nykyri et al.*, 2017].

The KH growth rate, Q, is determined by the unperturbed magnetospheric and magnetosheath conditions, which is given by *Chandrasekhar* [1961]:

$$(Q/k)^2 = a_1 a_2(\mathbf{\Delta v}\cdot\hat{\mathbf{k}})^2 - a_1(\mathbf{v_{A1}}\cdot\hat{\mathbf{k}})^2 - a_2(\mathbf{v_{A2}}\cdot\hat{\mathbf{k}})^2 \tag{5}$$

where k is the amplitude of wave vector, a_i is a density parameter for either side of the boundary defined by $a_i = \rho_i/(\rho_1 + \rho_2)$, $\Delta\mathbf{v}$ is the flow shear, $\mathbf{v_{Ai}}$ is the Alfvén velocity on either side, and $\hat{\mathbf{k}}$ is the unit wave vector. In principle, KH can operate in any direction that makes the right side of Equation 5 larger than zero, however, the wave vector direction which maximizes the growth rate will eventually dominate the process. Therefore, it is useful to quantify the KH instability by estimating the most unstable direction for this event by finding a direction of k that maximizes the growth rate $(Q/k)^2$. This is a standard maximization eigenvalue problem where we find the three eigenvector di-

	magnetosheath	magnetosphere
density (cm^{-3})	39.50	3.19
magnetic field (nT)	[−4.20, −13.13, 43.84]	[−17.90, −30.22, 23.35]
velocity ($km\,s^{-1}$)	[−171.68, −97.59, −18.36]	[−18.64, −26.77, 7.58]
temperature (eV)	78.4	1363

Table 1. Plasma properties and magnetic field in the unperturbed magnetosheath and magnetospheric side. The vectors are in GSE-coordinates. Calculation of typical magnetosheath and magnetospheric properties are computed using statistical entropy method (see text for details) and computed using FPI and FGM data between 18:55-20:05.

rections corresponding to maximum, intermediate and minimum eigenvalue. The eigenvector corresponding to the maximum eigenvalue is the direction of the most unstable k-vector, i.e., [-0.9084, +0.4179, -0.0115] in GSE coordinates, and has the associated growth speed, $Q/k = 26\,\mathrm{km\,s^{-1}} = 0.048\overline{V_f}$. For every direction for which the right-hand side of $(Q/k)^2$ is positive, the KHI could grow. To evaluate the portion of the total solid angle, $\Delta\Omega/\Omega = \Delta\Omega/4\pi = \Delta\varphi\Delta\theta/4\pi$ that is KHI unstable, we further evaluated the Q/k by sweeping all the directions with the finite increments of $d\varphi$, $d\theta$, where $d\varphi$ ranges from 0 to 2π and θ from 0 to π and then numerically integrated over all the angular increments, $\Delta\Omega$, that satisfied $(Q/k)^2 > 0$. This yields a total solid angle for wave vector directions that satisfy the KH onset condition (i.e., $\Delta\Omega = 0.3220 = 2.56\% \times 4\pi$), where $\overline{V_f}$ is the average of the fast mode speed $v_f = \sqrt{V_a^2 + c_s^2}$ between magnetosphere and magnetosheath, and c_s is the speed of sound. These parameters suggest a KH unstable boundary between magnetosheath and magnetosphere, but the KH mode can only propagate along a rather narrow direction. The relatively low growth rate means a relatively long-existing modified structure before the boundary has been fully diffused. This above estimation is based on plasma properties and magnetic field from the unperturbed magnetosphere and magnetosheath side (see Table 1), which is identified by the ion specific entropy, $S = T/n^{2/3}$. During the investigated interval between 18:55-20:05 UT, the ion specific entropy varies from about $5.7\,\mathrm{eV\,cm^2}$ in the magnetosheath side to about $699.5\,\mathrm{eV\,cm^2}$ in the magnetospheric side, which covers two orders of magnitude. Thus, we set $S < S_{msh} = \alpha \min(S)$ as magnetosheath plasma, and $S > \max(S)/\alpha$ as magnetospheric plasma, where $\alpha = \exp[5\% \times \log(\max(S)/\min(S))] = 1.2717$. Please note that Equation 5 is only applicable to an incompressible tangential discontinuity. *Merkin et al.* [2013] showed that at least in the low-latitude boundary layer, compressibility is an important factor for the KHI growth rate. The high-latitude boundary layer may be less compressible though. In our future work we will address the evaluation of the full *Miura and Pritchett* [1982] dispersion relation in the simulation of this event.

3.4 Burst Mode Analysis of Field-Aligned Wave Field Poynting Flux, Electron Heating and Plasma Wave Characteristics

Figure 6 shows MMS 3 burst mode observations of ion and electron perpendicular ($T_{i\perp}$ and $T_{e\perp}$) and parallel temperatures ($T_{i\parallel}$ and $T_{e\parallel}$)(panels a-d), and corresponding temperature ratios (e-f), and the electron pitch angle distributions at four different energy ranges: 0-200 eV (g), 200 eV-2 keV (h), 2-30 keV (i) and the 60-600 keV (j). The counter streaming electrons (with highest fluxes at 0 and 180 degree pitch angles) are evident both at low (g) and mid-energies (h).

The magnetic field strength and Alfvén speed are shown in panels k and l, respectively. The total and field-aligned wave-field Poynting flux between 1 Hz to 4096 Hz are shown in panels m and n, and the anomalous Ohmic heating (computed from $\mathbf{E} + \mathbf{v_e} \times \mathbf{B}) \cdot \mathbf{J}$) is shown in panel o. Both the KAWs and magnetosonic-whistler band waves can exist in this frequency range and can interact with the electrons, with whistler mode becoming more important at higher frequencies in the vicinity of the electron cyclotron frequency. The strong, 60 $\mu W/m^2$, mostly anti-field aligned (Earthward) Poynting flux peak at 19:46:57 is highlighted with the first yellow bar and coincides with the first, intense, counter-streaming electron -structure and local minima in the Alfvén speed (l). Note that Figure 4i showed Poynting flux for the background fields, while here the Poynting flux computation captures the energy carried by electromagnetic plasma waves in the range of 1-4096 Hz.

While the perpendicular ion to electron temperature ratio is in the range of ≈ 5-22, the parallel ratio varies from ≈1.5-8 and has local minimum in the regions of the strongest fluxes of counter streaming electrons and enhanced $T_{e\|}$ (see yellow vertical bars). The low energy, high-intensity counter-streaming electron fluxes and parallel temperature enhancements correlate with the magnitude of the field-aligned Poynting flux enhancements and enhanced anomalous Ohmic heating. This suggest that the Poynting flux in the range of 1-4096 Hz is associated with the parallel electron heating. Recent Hall-MHD and hybrid simulations demonstrate that anisotropic temperatures (both $T_\perp$ and $T_\|$ dominating) can be generated in the nonlinear stage of the KH instability in the different regions of the vortex, in which specific entropy and magnetic moment are not conserved [*Ma et al.*, 2019], and which may lead to wave generation due to available free energy. The enhanced fluxes of trapped (≈ 90 degree pitch angle) energetic electrons around 19:47 correspond to the stronger, large-scale magnetic field depression (see panel k and also Figure 2), while the enhanced fluxes of counter-streaming electrons correspond to more filamentary local depressions, which is consistent with the gyro-radius and diamagnetic effect. *Nykyri et al.* [2019a] recently showed that such pockets of energetic particles at high-latitudes close to exterior cusp could be created by low latitude reconnection when IMF is southward and has a strong y-component, which leads to a generation of magnetic bottle structures. For the present event, as IMF is northward, the pockets of trapped energetic electrons may be related to the magnetic bottle generation via magnetic reconnection driven by the KHI or are potentially generated during the previous interval of southward IMF. This will be a topic for our future study.

Figure 7 shows the analysis of the wave properties where the AC electric and magnetic field components are presented in the magnetic field-aligned coordinate (FAC) system between 19:46-19:49 in the frequency range of 1 to 4096 Hz (panels b-h) and shows background magnetic field (panel a) for guidance. In the field-aligned coordinate system the red color corresponds to component along the magnetic field, blue is the GSM (and GSE) x-axis, and the green component is computed from the cross-product and completes the coordinate system. The three solid black lines in panels d-g show (from top to bottom) the electron cyclotron frequency, ion plasma frequency, and lower hybrid frequency, respectively. Throughout the interval the electric field (panel b) fluctuations are mostly perpendicular to background magnetic field and have maximum amplitudes of ≈ 18 mV/m. The maximum power exists in the frequency range of ≈ 1-200 Hz (panel d) and they continue with lower power up to the electron cyclotron frequency, f_{ec}, (the top solid black line). The magnetic field (panel c) fluctuations (measured by SCM) show more variation in power with larger amplitudes starting at ≈19:46:57 and coinciding with the maximum field-aligned Poynting flux in Figure 6j. Also, at this time the magnetic field power density on panel e shifts towards higher frequencies while electric field fluctuations are more even throughout the period. The maximum magnetic field fluctuation amplitude is about 7 nT. The largest power fluctuations exist in the frequency range of 1-40 Hz and become smaller above the lower hybrid frequency. The ratio of the perpendicular electric field fluctuation power to the magnetic field fluctuation power $dE_\perp/dB_\perp$ is shown in panel f and normalized to local Alfvén speed (computed from the unfiltered SCM magnetic field) in panel g. This shows that the fluctuations appear to be electrostatic above the lower hybrid frequency and also during few intervals below the lower hybrid frequency where the magnetic field fluctuations have smaller amplitude. Please note that the fluctuations above 200 Hz are close to SCM noise level so the $dE_{\perp}/dB_{\perp}$ calculation may be less reliable above 200 Hz. The field-aligned Poynting flux (panel h), computed for each frequency bin from the wave electric and magnetic fields (FAC-system is defined using 0.1 s sliding window averaged burst mode FGM data), is largest between 1-40 Hz and gets smaller above the lower hybrid frequency, which is about 30 Hz. Interestingly, this is consistent with the median value of the characteristic heating frequency, which was computed with Equation 2 to be 21 Hz.

Figure 8 shows more wave characteristics for the same time interval together with the low energy electron pitch angle spectrogram (panel a), magnetic field strength (panel b) and the burst mode SCM magnetic field measurements in field-aligned coordinates (panel c) for providing context. Panels d-g present various unfiltered wave properties between 1-4096 Hz in spacecraft frame showing wave power spectrogram, degree of polarization for waves, wave propagation angle, and ellipticity. Wave properties are only shown for well polarized wave intervals for which polarization > 0.7.

The counter-streaming electrons correspond to the filamentary depressions in the magnetic field. Overall the wave properties are very patchy. Between 19:46:50 -19:47:00, corresponding to the intense Earthward (anti-field aligned) Poynting flux in Figure 6, there exists high powered, elliptically polarized, left-handed waves (in the spacecraft frame) in the range of 1 to 5 Hz (see the blue circle in panel g). The proton cyclotron frequency for 39-54 nT field (for the 19:46-19:49 time interval) is between $0.595 - 0.823$ Hz. These left-handed waves are further examined in the zoomed panel i) where the waveform is filtered between 1-32 Hz. It is clear that these 1-5 Hz waves exhibit a high degree of polarization with strong wave power. This interval is studied in detail, and waves identified via multi-spacecraft methods in the next section, because this corresponds to the largest anti-field aligned Poynting flux. However, there are also other left-hand polarized intervals at these frequencies with strong wave power and high degree of polarization, and that match the Poynting flux enhancements. These may belong to the same plasma wave branch.

Another interesting feature are the right-handed polarized waves at $\approx$ 19:48:35 (red circle in panel g), above the lower hybrid frequency and below the electron cyclotron and ion plasma frequency, that are further examined in panel h). These right-handed waves that exhibit high degree of polarization in the spacecraft frame propagate closely parallel to magnetic field and are associated with a peak of electron parallel temperature (see Figure 6 d). These are likely whistler waves.

The stripe-like structures in frequency space above 200 Hz are an artifact of the FFT due to sharp time domain structures below 32 Hz and disappear when the SCM data is filtered above 32 Hz. Figure 9 shows 0.8 seconds of four spacecraft measurements at 19:46:57.7 UT of the burst mode electric field and magnetic field components in GSE-coordinates, filtered between 32 Hz to 4096 Hz, and the corresponding Poynting flux calculations. The electric and magnetic field wave forms, and corresponding Poynting fluxes observed by four spacecraft are quite different (by visual inspection) suggesting that the wave-lengths are less than spacecraft separation of $\approx$ 30 km. Therefore the multi-spacecraft techniques [*Balikhin et al.*, 1997; *Dimmock et al.*, 2012; *Moore et al.*, 2016] may not be well suited for computing dispersion relation for these high frequency waves. Next we will apply a multi-spacecraft technique for calculating the experimental dispersion relation of the 0.16-16 Hz waves (which covers the ion cyclotron frequency) at 19:46:45-19:47:15 UT and compare it to the well known dispersion relations.

3.5 Plasma Wave Mode Identification Using a Two-spacecraft Method

In this section we use a well-established two-spacecraft method, utilizing wavelet transforms, to determine the k-vector of the waves at each frequency [*Balikhin et al.*, 1997; *Dimmock et al.*, 2013; *Moore et al.*, 2016]. We have performed the wave analysis using both SCM and FGM data, but the SCM data is more appropriate in resolving the peak amplitude of the ≈ 6 rad/s waves. The panel (a) of Figure 10 shows a 30 s interval of high resolution magnetic field data from MMS3 SCM instrumentation in the GSE coordinates at 19:46:45-19:47:15 UT, showing a series of wave packets. Panel (b) shows the SCM magnetic field in the local LMN coordinates by using MVA-B method, in which $\hat{\mathbf{L}} = [0.1049, -0.9885, -0.1085]$, $\hat{\mathbf{M}} = [0.9812, 0.0851, 0.1733]$, and $\hat{\mathbf{N}} = [-0.1621, -0.1247, 0.9789]$ in the GSE coordinates computed from the FGM data. The eigenvalue ratios are $\lambda_L/\lambda_M = 1.8139$, and $\lambda_M/\lambda_N = 1.7944$. Here, we choose the outward direction of $\hat{\mathbf{N}}$ such that $\hat{\mathbf{N}} \cdot \overline{\mathbf{B}}_{\text{FGM}} > 0$, where $\overline{\mathbf{B}}_{\text{FGM}} = [-13.0394, -20.0428, 38.8561]$nT is the average magnetic field from MMS3 and MMS4 FGM instrumentation. The panel (c) shows the angle between magnetic field $B_{L,M}$ components, $\phi = \arctan(B_L/B_M)$ for the MMS3 and MMS4. The increase of ϕ indicates that the wave is right-hand polarized, while the decrease of ϕ indicates a left-hand polarization.

Therefore, the wave roughly changes polarization three times during this time interval, and the polarization of the wave at MMS4 is mostly consistent with MMS3 before $t = 22$. The panel (d) shows the normalized cross-correlation of magnetic field B_L components from MMS3 and MMS4, which is given by $R(\delta t) = \int B_{L,4}(t) B_{L,3}(t - \delta t) dt$, and $\hat{R} = R/\max R$. The peak value at $\delta t = -30.9$ ms suggests the wave mainly propagated from MMS3 to MMS4.

We have decomposed the magnetic field B_x, B_y, and B_z from MMS3 and MM4 by using Morlet wavelet, $\mathbf{B}(t) \rightarrow \mathbf{A}(f, t)$, and zoomed into $t \in [5, 10]$s, which is highlighted by green shadows in panel (a)-(c). For each observed frequency in spacecraft frame, f_o, the wave vector direction $\hat{\mathbf{k}}(f_o)$ is the N direction from the MVA method based on the real part of $\mathbf{A}_3(f_o, t)$ and $\mathbf{A}_4(f_o, t)$, where the subscript refers to MMS3 and MMS4. The phase difference between MMS3 and MMS4, Φ_{43} is estimated based on the maximum wave amplitude $A = |A_{L3}|^2 + |A_{L4}|^2$ binned by $\Delta\Phi = \arg(A_{L4}) - \arg(A_{L3})$, where A_L is the L component of $\mathbf{A}$. Thus the amplitude of the wave vector can be estimated by $k(f_o) = \Phi_{43}/(\hat{\mathbf{k}}(f_o) \cdot \Delta\mathbf{R}_{43})$, where $\Delta\mathbf{R}_{43} = \mathbf{R}_4 - \mathbf{R}_3$, $\mathbf{R_3}$ and $\mathbf{R_4}$ are the location of MMS3 and MMS4 in the GSE coordinates. We fitted the $\hat{\mathbf{k}}(f_o)$, for the negative $k(f_o)$. The sign of $\mathbf{k} \cdot \Delta\mathbf{R}_{43}$ indicates whether the wave propagated from MMS3 to MMS4 or vice versa. Once the wave vector $\mathbf{k}(f_o)$ has been identified, one can estimate the plausible wave frequency in the plasma rest frame by using Appleton-Hartree (AH) equation (see for example *Bittecourt* [2004]),

$$\left(\frac{ck}{\omega}\right)^2 = 1 - \frac{X(1-X)}{1 - X - \frac{1}{2}Y^2\sin^2\theta \pm \sqrt{\left(\frac{1}{2}Y^2\sin^2\theta\right)^2 + (1-X)^2 Y^2 \cos^2\theta}} \tag{6}$$

Here, c is the speed of light, θ is the angle between $\mathbf{k}$ and background magnetic field, $X = \frac{\omega_{pe}^2}{\omega^2}$, $Y = \frac{\omega_{ge}}{\omega}$, $\omega_{pe} = 2.28 \times 10^5$ rad/s and $\omega_{ge} = 8.20 \times 10^3$ rad/s is the electron plasma frequency and electron gyro frequency, respectively, based on the background magnetic field 46.6 nT and electron density 16.4 cm^{-3}. In this study, the non-damped wave solutions are only associated with the negative sign. We also compared the experimental dispersion relation with that of the kinetic Alfvén wave [*Hasegawa*, 1976], which is given by

$$\omega^2 = k_\parallel^2 V_A^2 \left[1 + k_\perp^2 r_i^2 \left(1 + \frac{T_e}{T_i}\right)\right] \tag{7}$$

Here, r_i is the ion gyro-radius. The predicted angular wave frequency ω_p should transform from plasma rest frame into the spacecraft frame by including the Doppler effect,

$\omega_o(k) = 2\pi f_o(k) = \omega_p - \mathbf{k}\cdot\mathbf{U}$, where $\mathbf{U} = [-142.1158, -85.1102, -6.8525]$km/s is the plasma bulk velocity in the GSE coordinate during the green highlighted interval.

To provide a rough quantification of the wave polarization for each observed angular frequency ω_o during the given interval, we integrate all the positive angle changes between the magnetic field $B_{L,M}$ components, (i.e., $\Delta_i\phi(\omega_o) = \phi(\omega_o, t_{i+1}) - \phi(\omega_o, t_i) > 0$) , and normalized by the total magnetic field B_{LM} component angle change $|\Delta_i\phi(\omega_o)|$, that is

$$\sigma(\omega_o) = \frac{\sum_{>0}\Delta_i\phi(\omega_o)}{\sum|\Delta_i\phi(\omega_o)|} \tag{8}$$

where the subscript i refers to the i-th measurement. Thus, the σ close to 1 indicates right-hand polarization, and value close to 0 means left-hand polarization. The delay time from cross-correlation of magnetic field $B_L(\omega_o)$ components from MMS3 and MMS4 are also estimated to compare with the phase analysis results.

The panel (e) of Figure 10 plots the wave amplitude $\int A(\omega_0, t)dt$ as a function of the observed frequency, ω_o, showing two energy peaks at $\omega_o = 6.3794$ rad/s and 11.1072 rad/s. The data are color coded by σ, suggesting that most of the waves are left-hand polarized in the spacecraft frame. The panel (f) of Figure 10 shows the predicted wave frequency with doppler shift vs. the observed wave frequency. To show the polarization in the plasma frame, we flipped the polarization if the doppler shift changes the sign of the angular frequency. The solid blue line indicates when the predicted value is equal to the observation, and the two dashed blue lines represent 50% deviation. For each data point, we only present the dispersion relation which is more close to the observed frequency, in which diamond marker represents the AH equation and the circle marker represents the KAW. All markers are color coded by the wave amplitude, A, suggesting that the predicted frequency of the large-amplitude waves mostly agrees with the observation. The red plus signs indicate that $\mathbf{k}\cdot\Delta\mathbf{R}_{43} > 0$ and the cross-correlation analysis provides consistent results for the wave propagation direction, for majority of the cases. The red cross signs indicate that the two methods give inconsistent results. The size of red signs represents the eigenvalue ratio λ_M/λ_N. Most of the red signs are larger than the marker size, meaning $\lambda_M/\lambda_N > 2$.

The above wave analysis shows that frequency at $\omega = 6.84\,\mathrm{rad\,s^{-1}}$ which has a wave vector, $\mathbf{k} = [0.0124, 0.0108, 0.0278]\mathrm{km}^{-1}$, fits the KAW dispersion relation very well. The wave length perpendicular to magnetic field is $\lambda_\perp = 2\pi/k_\perp = 215$ km.

We have performed the analysis using all the spacecraft pairs (see Supplementary Information). Figure 11 presents MMS constellation and separations relative to k-vector of the observed waves. The big dots represent the location of the four MMS spacecraft in red (1), green (2), blue (3), and black (4), respectively. The arrows indicate the direction of the wave vectors corresponding to the largest wavelet amplitudes for each pair of spacecraft, which are labeled in the middle of each pair of spacecraft. It can be seen that MMS3 and MMS4 were mostly aligned along the KAW wave vector direction providing the best result. Repeating the analysis using FGM data (see Supplementary Figure S6) gives smaller amplitude and larger error for the 6.84 rad/s KAW peak, but in addition it also shows a large amplitude ≈ 2 rad/s right-handed peak that also satisfies the KAW dispersion relation. KAWs can have both left and right-hand polarizations in the plasma frame [*Hunana et al.*, 2013].

To better understand the dynamics of these boundary layer wave observations relative to MMS, it is useful to consider the angles between the various wave vectors and background magnetic field. The angle between the KH wave k-vector direction ($\mathbf{k}_{KH}$ = [-0.9084, 0.4179, -0.0115]) and the well defined KAW k-vector direction ($\mathbf{k}_{KAW}$ = [0.383910, 0.334373, 0.860702]), as detected by the MMS3 and MMS4, is ≈ 100 degrees. The KH wave and the KAW propagate at angles of ≈ 86 and 62 degrees relative to background magnetic field direction ($\hat{\mathbf{B}}_{\mathbf{FGM}}$ = [-0.285795, -0.439307, 0.851663]), respectively.

The background magnetic field was determined from the average of MMS3 and MMS4 FGM- observations during the KAW observation. Figure 12a shows a KH simulation and schematic using Hall-MHD code described in *Nykyri and Otto* [2004] and in Supplementary Information. The purpose of this simulation is to illustrate how sharp Alfvén speed (V_A) gradients can be generated by the KHI. The background color shows the Alfvén speed which is larger on the magnetospheric (yellow) than on the magnetosheath (blue) side. Virtual spacecraft time-series measurements of the Alfvén speed during the simulation are shown with black trace which matches the MMS observations shown in Figure 4. The KH wave wavelength in the simulation is 4.4 R_E which results in $\approx$ 4 minute period between the maximum gradients in the Alfvén speed, also observed in Figure 4 (see the first two purple vertical columns). Figure 12b shows the KAW which was observed at the gradient of the Alfvén speed indicated by the yellow box in panel a. Figure 12c shows the schematic summarizing these high-latitude boundary layer observations, with the directions of the KH wave and KAW **k**-vectors superposed onto Tsyganenko 96 magnetic field lines (also shown in Figure 1), together with the observed magnetic field direction (green vector). The four MMS spacecraft (labeled 1-4 inside colored circles) separations are over-magnified to illustrate the consistency of the magnetic field topology with respect to KH wave propagation direction, and emission of the KAW at the Alfvén velocity gradient and its propagation mostly along the MMS3 and MMS4 separation vector direction.

3.6 Evaluating Electron heating by the Kinetic Alfvén Waves (KAWs)

Since we have now "fingerprinted" the plasma wave mode as KAW, we can evaluate its effectiveness on electron heating. Electrons could be accelerated in the parallel electric field of a KAW. With electric fields defined in terms of the parallel (ψ) and perpendicular (ϕ) potentials as described in *Hasegawa* [1976]:

$$E_{\parallel} = -k_{\parallel}\psi \tag{9}$$
$$E_{\perp} = -ik_{\perp}\phi \tag{10}$$

We should expect that in a KAW electrons would be accelerated along the magnetic field to an energy

$$U \approx e\psi \tag{11}$$

For a KAW

$$\psi = -(T_e/T_i)(k_{\perp}\rho_i)^2\phi \tag{12}$$
$$\approx (T_e/T_i)(k_{\perp}\rho_i)^2 E_{\perp}/k_{\perp} \tag{13}$$

We use here the measured values during KAW observation at 19:46:45-19:47:15 UT where $T_e/T_i = 0.1305$ (average electron to ion temperature ratio), $\rho_i = 30.9\,\mathrm{km}$ (ion thermal gyroradius), $k_{\perp} = 0.0292\,\mathrm{km}^{-1}$ (perpendicular wave number), $\max E_{\perp} = 1.5484\,\mathrm{mV\,m}^{-1}$ (maximum perpendicular electric field), which yield the maximum parallel potential $\psi_{\max} \approx 5.6449\,\mathrm{V}$. The expected electron energization in the identified KAW electric field is therefore about 5.6 eV. This value is smaller than the KAW parallel potential of $\approx$100 V in *Lee et al.* [1994], which was estimated using typically observed Alfvén speed, perpendicular magnetic field fluctuation amplitude, and estimated parallel wave length instead of the measured $E_{\perp}/k_{\perp}$. Note that here the MMS separation of 30 km is appropriate for estimating the KAW perpendicular wave length of 215 km. Assuming that the KAW spectrum continues to $k_{\perp} = 1/\rho_i$ =0.032/km and using the maximum electric field amplitude of $\approx 15\,\mathrm{mV\,m}^{-1}$ at 19:46:57, would yield a potential of about 60 V. The highest fluxes of counter-streaming electrons at the outer boundary layer (see Figure 6g and h, and panel 4 in Figure 2) have energies from $\approx$ ten eV to $\approx$ 100 eV.

To evaluate the electron heating by bounce resonance with the kinetic Alfvén waves, we use the equation from the quasi-linear theory [*Hasegawa and Mima*, 1978], in which the parallel heating rate, dT_e/dt is given by:

$$dT_e/dt = T_e \omega G, \tag{14}$$

where ω is the angular frequency of the surface wave, which can be estimated from spectra shown in Figure 5 to be $2\pi \times 0.01\,\mathrm{rad\,s^{-1}}$, $G = \sqrt{\frac{\pi}{8}} \frac{m_i}{m_e} \sum_k \frac{|\delta B_{\perp k}|^2}{|B_0|^2} F(x) H(\lambda_s)$, $H(\lambda_s) = \frac{\lambda_s}{(1+\lambda_s)^{3/2}}$, $F(x) = x^3 \exp(-x^2/2)$, $x = v_A/v_{T_e}$, $\lambda_s = (k_\perp \rho_s)^2$, $\rho_s = T_e/T_i \rho_i$, and ρ_i is the ion gyro-radius. For a time-independent G, $T_e = T_{e0} \exp(t\omega G)$. Note that $F(x) \leq 1.1582$, and $H(\lambda_s) \leq 0.3859$, and one can easily estimate that $G \leq 487|\delta B_\perp/B_0|^2$. In this event, assuming all perturbation is KAW wave, $|\delta B_\perp/B_0| \approx 0.025$, G is less than 0.3. Thus, from Equation 14, the time-scale for parallel heating of electrons from 18 eV (value of $T_{e\|}$ in the magnetosheath at ≈19:59 UT) to 55 eV (maximum values observed at the heated boundary layer shown in Figure 6), Δt is at least

$$\Delta t = \ln(\frac{55\,\mathrm{eV}}{18\,\mathrm{eV}})/(2\pi \times 0.01 \times 0.3) = 59.3\,\mathrm{s} \tag{15}$$

As a comparison, this time scale is much longer than the characteristic heating time of $1/21$ Hz $= 0.047$ s computed from the entropy equation 2, indicating that the KAWs provide a rather small non-adiabatic heating source compared to the overall processes in this case.

4 Conclusions and Discussion

In this paper we have analyzed MMS observations at the high-latitude boundary layer where MMS encountered quasi-periodic variations in all plasma quantities, as well as parallel heated low energy (0-2 keV) electrons, and energetic (70-600 keV) ions and electrons. The present work was motivated by the observations of multi-scale wave structures (spanning from few minutes, to typical ion and electron frequencies) observed at the vicinity of the dawn-sector southern cusp in association with counter-streaming, low-energy electrons and trapped high energy electrons. The multi-spacecraft observations and high time-cadence electric and magnetic field observations allowed us to identify some of the waves and quantify their effectiveness on the non-adiabatic heating. We can summarize our main findings as follows:

1. The frequency analysis of the low frequency (75 -100 s) fluctuations between 19:40-20:05 UT, growth rate calculations, finite unstable solid angle range and local 2.5-D simulations suggest this is a high-latitude KH event with a wave length of about 3-5 R_Es.

2. The parallel electron temperature enhancements were associated with enhanced magnitude of field-aligned Poynting flux. The most intense anti-field aligned Poynting flux was carried by the large amplitude kinetic Alfvén waves (KAWs) with perpendicular wave lengths of about 200 km at the gradient of the Alfvén speed (see Figures 4h and 12) consistent with the previous observations of mode conversion [*Chaston et al.*, 2007]. One of the KAW modes has been unambiguously identified in terms of experimental dispersion relation using two-spacecraft wavelet analysis method. The parallel potential associated with this mode was about 6V and thus not sufficient to explain the origin of the > 100 eV counter streaming electrons.

3. In order to evaluate a typical time-scale of the heating of the boundary layer we derived the equation for the *characteristic heating frequency*, f_{heat}, utilizing equations for plasma entropy and pressure, and Hall-MHD plasma approximation. The median f_{heat} was evaluated to be 21 Hz. This indicates a rapid heating of the boundary layer.

4. The resonant heating associated with the identified KAW spectrum was evaluated to be ≈ 60 seconds and thus too slow to account for all the observed heating during the present event.

5. Our analysis is indicative that the low frequency fluctuations were likely KH waves that were created by the velocity shear at the high-latitude boundary layer. These compressional KH waves can mode convert and create KAWs [*Johnson et al.*, 2001; *Chaston et al.*, 2007] which can carry significant Poynting flux into the ionosphere. While for the identified KAW spectrum the wave energy was able to provide some of the parallel heating of the electrons, the observed values of $E_\perp$ and $k_\perp$ were not to sufficient to explain all of the rapid, non-adiabatic heating when transitioning from the magnetosheath into the magnetosphere. This suggests that additional processes (e.g., other plasma wave modes, turbulence or electric fields associated with magnetic reconnection) must also play role and provide heating during the present event.

6. One potential source for both ion and electron heating are the magnetosonic-whistler branch waves. For the present event MMS observed right-hand polarized waves (in spacecraft frame) at ≈ 19:48:35, just above the lower hybrid frequency (about 30 Hz) that were associated with parallel electron heating. These could potentially be whistler waves. The median value of the characteristic heating frequency of 21 Hz would be more consistent with the whistler-branch waves (assuming electrons could be heated in few wave cycles).

7. The anomalous Ohmic heating rate was strongly varying from -1.5 to + 1μW/m^3, during the KAW interval at ≈ 19:46:45 (see Figure 6o), and much larger than the variation during the potential whistler wave emission at 19:48:35. This strong variation (in sign) in anomalous Ohmic heating can indicate strong wave-particle interactions between electrons and KAW wave field.

The counter-streaming, bi-directional low-energy electrons in the vicinity of the magnetopause have been frequently observed both by Cluster [*Vines et al.*, 2017] and MMS [*Fuselier et al.*, 2017] in association with magnetic islands and multiple X-lines that can be formed by magnetic reconnection. Also, the anti-parallel or component reconnection occurring at the northern and southern hemisphere at the similar time could potentially lead to bi-directional electrons [*Fuselier et al.*, 2011, 2012]. However, for the prevailing IMF orientation (B_z positive and B_y negative) we do not expect either the component reconnection at the low-latitudes or high-latitude reconnection in the vicinity of the southern cusp at the dawn-sector to directly operate.

While the anti-parallel reconnection could operate at the dusk sector in the vicnity of the northern cusp, it would not explain the bi-directional electrons at the dawn sector of the southern cusp. One likely possibility is the mid-latitude reconnection occurring ≈ 2-3 R_E above and below the shear-flow plane in association with the 3-D KHI [*Ma et al.*, 2017; *Hwang et al.*, 2020] which can generate a magnetic island and lead to potentially counter-streaming low-energy electron observations along spacecraft trajectory at shear flow plane between these two reconnection sites. Recently, another MMS event showed counter-streaming electrons at high-latitude magnetopause likely generated by the KHI driven reconnection [*Burkholder et al.*, 2020a]. A constellation of spacecraft both below, above and close to instability shear-flow plane containing the most unstable k-vector direction, and spanning the fluid (≈ 0.5-6 R_E), ion (≈ 70-3000 km) and ion-electron hybrid scales (1-70 km) would be required to unambiguously identify this process, e.g., from pre-existing boundary layer with bi-directional electrons.

The generated small scale processes have in turn impact on the plasma properties that affect the large scale processes. For KHI these "cross-scale couplings" would arise during typical KH growth time from linear to non-linear, and to the highly rolled up stage. The small-scale processes (such as reconnection in the vortices [*Nykyri and Otto*, 2004; *Hasegawa et al.*, 2009; *Eriksson et al.*, 2016; *Li et al.*, 2016]) diffuse the sharp velocity boundary layer, so that sources of free energy capable for exciting the same-wavelength (macroscopic) KH wave get reduced as the fastest growing KH wavelength has wavelength proportional to the velocity shear layer thickness [*Miura and Pritchett*, 1982]. At the low latitudes a subsequent interval of southward IMF (after northward IMF) would be needed to re-create thin boundaries at the KHI source region before the same wavelength KH wave can be re-created. The 3-D MHD simulation studies have shown that in the nonlinear stage, both magnetic reconnection and KH modes mutually impact the onset and operating conditions of each other by changing the width of the transition layer, i.e., the current layer and the shear-flow layer. The normalized magnetic reconnection rate is strongly increased by the nonlinear KH waves; however, these waves also limit the total reconnected flux by dissipating the electric current when the largest wavelength mode becomes highly nonlinear. This interaction leads to fast reconnection with local rates that are equal to the Petschek rate of fast reconnection without invoking Hall physics [*Ma et al.*, 2014a,b]. Also, the kinetic scale waves generated by the KHI [*Moore et al.*, 2016] or reconnection [*Graham et al.*, 2017] can give energy to the plasma particles, increasing their gyroradius leading to more effective diffusion which in turn can diffuse the boundary layer more effectively to reduce the sources of free energy.

We will return in our future work to quantify the heating from these other processes (when spacecraft separations are appropriate) as well as study the formation mechanisms of the trapped high-energy (70-600 keV) electrons and protons with help of numerical simulations. *Nykyri et al.* [2019a] recently showed that such pockets of energetic particles at high-latitudes close to exterior cusp could be created by low latitude reconnection when IMF is southward and has a strong y-component, which can lead to a generation of magnetic bottle structures. Magnetic bottles in the vicinity of the exterior cusps can also be created by high-latitude reconnection [*Nykyri et al.*, 2011a,b, 2012; *Adamson et al.*, 2011, 2012]. For the present event, as the IMF is northward, the pockets of trapped energetic electrons may be related to 1) the magnetic bottle generation via magnetic reconnection driven by the KHI or 2) are potentially generated during the previous intervals of southward IMF via low latitude reconnection [*Nykyri et al.*, 2019a], or 3) due to previous IMF conditions favoring high-latitude reconnection [*Nykyri et al.*, 2011a]. Ions are less adiabatic than electrons and have a larger gyro-radius which may explain why the 70-600 keV ions for the present event are frequently in the loss cone while electrons remain trapped. The mostly field-aligned component of high-energy ions suggest that these particles can be lost from the magnetosphere to the magnetosheath. Recently, *Cohen et al.* [2017] reported a statistical study of the leaked $\approx$ 40 keV electrons in the magnetosheath, which may be related to the "opening" of the magnetic bottle structures due to changing IMF orientation or KHI driven dynamics.

Finally, we note that during the present event magnetosphere is embedded in a slow solar wind, manifested both by its low speed ($\approx$ 300 km/s) and high density ($\approx$ 15/cc). In such magnetopause configuration, our KH onset condition analysis (Equation 6) estimates a low KH growth rate along a very narrow direction even without considering finite initial shear flow width and compressibility, which could further stabilize the magnetopause [*Miura and Pritchett*, 1982]. Therefore, we cannot fully rule out that the observed low-frequency magnetopause waves at KH frequencies could be surface waves excited by upstream disturbances rather than the velocity shear [*Plaschke et al.*, 2013]. For example, the magnetosheath jets originating from quasi-parallel shock can generate negative B_z in the magnetosheath even during northward IMF [*Nykyri et al.*, 2019b], which could drive transient dayside reconnection [*Hietala et al.*, 2018] and also generate surface waves. Exploring these other possibilities for generation of these low frequency waves would be a natural extension of the work presented above.

A: Appendix: Derivation of the Characteristic Heating Frequency

Specific entropy is defined as

$$S = \rho^{-\gamma} P, \tag{A.1}$$

where P is the plasma thermal pressure, ρ is the plasma density, and $\gamma = 5/3$ is the ratio of specific heats. The total time derivative of specific entropy is:

$$dS/dt = \rho^{-\gamma} dP/dt + P d\rho^{-\gamma}/dt. \tag{A.2}$$

$$\tag{A.3}$$

Using the definition of the plasma pressure equation (see e.g., *Otto* [1990]),

$$\frac{1}{\gamma - 1}\left(\frac{\partial}{\partial t}P + \nabla \cdot P\mathbf{u}\right) = -P\nabla \cdot \mathbf{u} + \eta \mathbf{j}^2, \tag{A.4}$$

where $\mathbf{u}$ is the plasma velocity, $\mathbf{J}$ is the current density, and taking the total time derivative of P,

$$\frac{dP}{dt} = \frac{\partial P}{\partial t} + \mathbf{u} \cdot \nabla P, \tag{A.5}$$

$$\tag{A.6}$$

the Equation A.4 can be re-organized as follows,

$$\frac{dP}{dt} + P\nabla \cdot \boldsymbol{u} = -(\gamma - 1) P\nabla \cdot \boldsymbol{u} + (\gamma - 1)\eta \boldsymbol{j}^2 \tag{A.7}$$

$$\frac{dP}{dt} = -\gamma P\nabla \cdot \boldsymbol{u} + (\gamma - 1)\eta \boldsymbol{j}^2. \tag{A.8}$$

Using the mass continuity equation and the total time derivative of the plasma mass density,

$$\frac{\partial \rho}{\partial t} + \nabla \cdot \rho\mathbf{u} = 0 \tag{A.9}$$

$$\frac{d\rho}{dt} = -\rho\nabla \cdot \boldsymbol{u}, \tag{A.10}$$

the equation A.2 can be transformed to,

$$\frac{d}{dt}\left(\frac{P}{\rho^\gamma}\right) = \frac{1}{\rho^\gamma}\frac{dP}{dt} - \gamma\frac{P}{\rho^{\gamma+1}}\frac{d\rho}{dt} \tag{A.11}$$

$$= \frac{1}{\rho^\gamma}\left(\frac{dP}{dt} - \gamma\frac{P}{\rho}\frac{d\rho}{dt}\right) \tag{A.12}$$

$$= \frac{1}{\rho^\gamma}\left[-\gamma P\nabla \cdot \boldsymbol{u} + (\gamma - 1)\eta \boldsymbol{j}^2 - \gamma\frac{P}{\rho}(-\rho\nabla \cdot \boldsymbol{u})\right] \tag{A.13}$$

$$= \frac{1}{\rho^\gamma}\left[-\gamma P\nabla \cdot \boldsymbol{u} + (\gamma - 1)\eta \boldsymbol{j}^2 + \gamma P\nabla \cdot \boldsymbol{u}\right] \tag{A.14}$$

$$= \frac{(\gamma - 1)}{\rho^\gamma}\eta \boldsymbol{j}^2 \tag{A.15}$$

$$\rightarrow \tag{A.16}$$

$$\frac{dS}{dt} = (\gamma - 1)\frac{\eta J^2}{\rho^\gamma}, \tag{A.17}$$

Dividing both sides with S, leads to an equation with units in 1/time, and is named as the equation for the characteristic heating frequency, f_{heat}:

$$f_{heat} = \frac{1}{S}\frac{dS}{dt} = \frac{\eta J^2}{P/(\gamma - 1)}. \tag{A.18}$$

The right hand side of the equation 2 is the Ohmic heating (ηJ^2) to plasma thermal energy density ($P/(\gamma - 1)$) ratio.

Acknowledgments

The work performed by KN, EK, PD and JJ were supported by NASA grant #NNX17AI50G. The work performed by KN and RR was supported by NSF grant #1707521. The work supported by BB was supported by NASA grant # 80NSSC8K1381. The work performed by XM was supported by NASA grant #NNX16AF89G. AM, KS, and VM were supported by NASA grant # 80NSSC8K1381 via a subcontract to JHU/APL. DL was supported by the Advanced Study Program Postdoctoral Fellowship of the National Center for Atmospheric Research. The French (LPP) involvement for the SCM instrument is supported by CNES and CNRS. All MMS data were downloaded through the MMS Science Data Center accessible at https://lasp.colorado.edu/mms/sdc/public/, and we recognize the efforts from MMS instrument teams and all who contribute to this service. The simulation data and visualization tools in this paper can be accessed from https://commons.erau.edu/. We acknowledge use of NASA/GSFC's Space Physics Data Facility's OMNIWeb (http://omniweb.gsfc.nasa.gov) service and Orbit Visualization Tool (https://ovt.irfu.se).

References

Adamson, E., A. Otto, and K. Nykyri (2011), 3-D mesoscale MHD simulations of a cusp-like magnetic configuration: method and first results, *Annales Geophysicae*, *29*, 759–770, doi:10.5194/angeo-29-759-2011.

Adamson, E., A. Otto, and K. Nykyri (2012), 3-D mesoscale MHD simulations of magnetospheric cusp-like configurations: cusp diamagnetic cavities and boundary structure, *Annales Geophysicae*, *30*, 325–341, doi:10.5194/angeo-30-325-2012.

Balikhin , M. A., T. D. de Wit, H. S. C. K. Alleyne, L. J. C. Woolliscroft, S. N. Walker, V. Krasnosel'skikh, W. A. C. Mier-Jedrzejeowicz, and W. Baumjohann (1997), Experimental determination of the dispersion of waves observed upstream of a quasi-perpendicular shock, *Geophys. Res. Lett.*, *24*, 787–790, doi:10.1029/97GL00671.

Belmont, G., F. Reberac, and L. Rezeau (1995), Resonant amplification of magnetosheath MHD fluctuations at the magnetopause, *Geophysical Research Letters*, *22*, 295–298, doi:10.1029/94GL03078.

Bittecourt, J. A. (2004), *Fundamentals of Plasma Physics*, 3 ed., Springer-Verlag New York, The address.

Blake, J. B., B. H. Mauk, D. N. Baker, P. Carranza, J. H. Clemmons, J. Craft, W. R. Crain, A. Crew, Y. Dotan, J. F. Fennell, R. H. Friedel, L. M. Friesen, F. Fuentes, R. Galvan, C. Ibscher, A. Jaynes, N. Katz, M. Lalic, A. Y. Lin, D. M. Mabry, T. Nguyen, C. Pancratz, M. Redding, G. D. Reeves, S. Smith, H. E. Spence, and J. Westlake (2016), The Fly's Eye Energetic Particle Spectrometer (FEEPS) Sensors for the Magnetospheric Multiscale (MMS) Mission, *Space Science Reviews*, *199*, 309–329, doi:10.1007/s11214-015-0163-x.

Borovsky, J. E., and T. E. Cayton (2011), Entropy mapping of the outer electron radiation belt between the magnetotail and geosynchronous orbit, *Journal of Geophysical Research (Space Physics)*, *116*, A06216, doi:10.1029/2011JA016470.

Burch, J. L., T. E. Moore, R. B. Torbert, and B. L. Giles (2016), Magnetospheric Multiscale Overview and Science Objectives, *Space Science Reviews*, *199*, 5–21, doi:10.1007/s11214-015-0164-9.

Burkholder, B., K. Nykyri, X. Ma, R. Rice, S. A. Fuselier, K. Trattner, K. R. Pritchard, J. L. Burch, and S. M. Petrinec (2020a), Magnetospheric Multi-Scale Observations of an Electron Diffusion Region at High-Latitudes, *Geophysical Research Letters*, *xx*, under minor revision.

Burkholder, B. L., P. A. Delamere, J. R. Johnson, and C.-S. Ng (2020b), Identifying active kelvin–helmholtz vortices on saturn's magnetopause boundary, *Geophysical Re-*

search Letters, *47*(1), e2019GL084,206, doi:10.1029/2019GL084206, e2019GL084206 10.1029/2019GL084206.

Chandrasekhar, S. (1961), *Hydrodynamic and Hydromagnetic Stability*, Oxford Univ. Press, New York.

Chaston, C., J. Bonnell, J. P. McFadden, C. W. Carlson, C. Cully, O. Le Contel, A. Roux, H. U. Auster, K. H. Glassmeier, V. Angelopoulos, and C. T. Russell (2008), Turbulent heating and cross-field transport near the magnetopause from themis, *Geophysical Research Letters*, *35*(17), doi:10.1029/2008GL033601.

Chaston, C. C., T. D. Phan, J. W. Bonnell, F. S. Mozer, M. Acuńa, M. L. Goldstein, A. Balogh, M. Andre, H. Reme, and A. Fazakerley (2005), Drift-Kinetic Alfvén Waves Observed near a Reconnection X Line in the Earth's Magnetopause, *Physical Review Letters*, *95*(6), 065002, doi:10.1103/PhysRevLett.95.065002.

Chaston, C. C., M. Wilber, F. S. Mozer, M. Fujimoto, M. L. Goldstein, M. Acuna, H. Reme, and A. Fazakerley (2007), Mode Conversion and Anomalous Transport in Kelvin-Helmholtz Vortices and Kinetic Alfvén Waves at the Earth's Magnetopause, *Physical Review Letters*, *99*(17), 175004, doi:10.1103/PhysRevLett.99.175004.

Chaston, C. C., J. R. Johnson, M. Wilber, M. Acuna, M. L. Goldstein, and H. Reme (2009), Kinetic Alfvén Wave Turbulence and Transport through a Reconnection Diffusion Region, *Physical Review Letters*, *102*(1), 015001, doi: 10.1103/PhysRevLett.102.015001.

Cohen, I. J., B. H. Mauk, B. J. Anderson, J. H. Westlake, D. G. Sibeck, D. L. Turner, J. F. Fennell, J. B. Blake, A. N. Jaynes, T. W. Leonard, D. N. Baker, H. E. Spence, G. D. Reeves, B. J. Giles, R. J. Strangeway, R. B. Torbert, and J. L. Burch (2017), Statistical analysis of MMS observations of energetic electron escape observed at/beyond the dayside magnetopause, *Journal of Geophysical Research: Space Physics*, *122*(9), 9440–9463, doi:10.1002/2017JA024401, 2017JA024401.

Cowee, M. M., D. Winske, and S. P. Gary (2009), Two-dimensional hybrid simulations of superdiffusion at the magnetopause driven by Kelvin-Helmholtz instability, *Journal of Geophysical Research (Space Physics)*, *114*, A10209, doi:10.1029/2009JA014222.

De Keyser, J., M. Roth, F. Reberac, L. Rezeau, and G. Belmont (1999), Resonant amplification of MHD waves in realistic subsolar magnetopause configurations, *Journal of Geophysical Research*, *104*, 2399–2410, doi:10.1029/1998JA900060.

Delamere, P. A., R. J. Wilson, and A. Masters (2011), Kelvin-Helmholtz instability at Saturn's magnetopause: Hybrid simulations, *Journal of Geophysical Research (Space Physics)*, *116*, A10222, doi:10.1029/2011JA016724.

Dimmock, A. P., M. A. Balikhin, V. V. Krasnoselskikh, S. N. Walker, S. D. Bale, and Y. Hobara (2012), A statistical study of the cross-shock electric potential at low mach number, quasi-perpendicular bow shock crossings using cluster data, *Journal of Geophysical Research (Space Physics)*, *117*, 2210, doi:10.1029/2011JA017089.

Dimmock, A. P., M. A. Balikhin, , S. A. Walker, and Pope (2013), Dispersion of low frequency plasma waves upstream of the quasi-perpendicular terrestrial bow shock, *Annales Geophysicae*, *31*.

Dimmock, A. P., K. Nykyri, H. Karimabadi, A. Osmane, and T. I. Pulkkinen (2015), A statistical study into the spatial distribution and dawn-dusk asymmetry of dayside magnetosheath ion temperatures as a function of upstream solar wind conditions, *Journal of Geophysical Research (Space Physics)*, *120*, 2767–2782, doi:10.1002/2014JA020734.

Dimmock, A. P., K. Nykyri, A. Osmane, H. Karimabadi, and T. I. Pulkkinen (2017), *Dawn-Dusk Asymmetries of the Earth's Dayside Magnetosheath in the Magnetosheath Interplanetary Medium Reference Frame*, chap. 5, pp. 49–72, American Geophysical Union (AGU), doi:10.1002/9781119216346.ch5.

Drake, J. F., R. G. Kleva, and M. E. Mandt (1994), Structure of thin current layers: Implications for magnetic reconnection, *Physical Review Letters*, *73*, 1251–1254, doi: 10.1103/PhysRevLett.73.1251.

Dungey, J. W. (1961), Interplanetary magnetic field and the auroral zones, *Phys. Rev. Lett.*, *6*, 47–48, doi:10.1103/PhysRevLett.6.47.

Ergun, R. E., S. Tucker, J. Westfall, K. A. Goodrich, D. M. Malaspina, D. Summers, J. Wallace, M. Karlsson, J. Mack, N. Brennan, B. Pyke, P. Withnell, R. Torbert, J. Macri, D. Rau, I. Dors, J. Needell, P.-A. Lindqvist, G. Olsson, and C. M. Cully (2016), The Axial Double Probe and Fields Signal Processing for the MMS Mission, *Space Science Reviews*, *199*, 167–188, doi:10.1007/s11214-014-0115-x.

Eriksson, S., B. Lavraud, F. D. Wilder, J. E. Stawarz, B. L. Giles, J. L. Burch, W. Baumjohann, R. E. Ergun, P.-A. Lindqvist, W. Magnes, C. J. Pollock, C. T. Russell, Y. Saito, R. J. Strangeway, R. B. Torbert, D. J. Gershman, Y. V. Khotyaintsev, J. C. Dorelli, S. J. Schwartz, L. Avanov, E. Grimes, Y. Vernisse, A. P. Sturner, T. D. Phan, G. T. Marklund, T. E. Moore, W. R. Paterson, and K. A. Goodrich (2016), Magnetospheric Multiscale observations of magnetic reconnection associated with Kelvin-Helmholtz waves, *Geophys. Res. Lett.*, *43*, 5606–5615, doi:10.1002/2016GL068783.

Fairfield, D. H., A. Otto, T. Mukai, S. Kokubun, R. P. Lepping, J. T. Steinberg, A. J. Lazarus, and T. Yamamoto (2000), Geotail observations of the Kelvin-Helmholtz instability at the eqatorial magnetotail boundary for parallel northward fields, *J. Geophys. Res.*, *105*, 21,159–21,174.

Fujimoto, M., and T. Terasawa (1994), Anomalous ion mixing within an MHD scale Kelvin-Helmholtz vortex, *J. Geophys. Res.*, *99*, 8601–8614.

Fuselier, S. A., K. J. Trattner, and S. M. Petrinec (2011), Antiparallel and component reconnection at the dayside magnetopause, *Journal of Geophysical Research: Space Physics*, *116*(A10), doi:10.1029/2011JA016888.

Fuselier, S. A., K. J. Trattner, S. M. Petrinec, and B. Lavraud (2012), Dayside magnetic topology at the earth's magnetopause for northward imf, *Journal of Geophysical Research: Space Physics*, *117*(A8), doi:10.1029/2012JA017852.

Fuselier, S. A., S. K. Vines, J. L. Burch, S. M. Petrinec, K. J. Trattner, P. A. Cassak, L.-J. Chen, R. E. Ergun, S. Eriksson, B. L. Giles, D. B. Graham, Y. V. Khotyaintsev, B. Lavraud, W. S. Lewis, J. Mukherjee, C. Norgren, T.-D. Phan, C. T. Russell, R. J. Strangeway, R. B. Torbert, and J. M. Webster (2017), Large-scale characteristics of reconnection diffusion regions and associated magnetopause crossings observed by mms, *Journal of Geophysical Research: Space Physics*, *122*(5), 5466–5486, doi:10.1002/2017JA024024.

Fuselier, S. A., K. J. Trattner, S. M. Petrinec, M. H. Denton, S. Toledo-Redondo, M. André, N. Aunai, C. R. Chappell, A. Glocer, S. E. Haaland, M. Hesse, L. M. Kistler, B. Lavraud, W. Li, T. E. Moore, D. Graham, L. Alm, P. Tenfjord, J. Dargent, S. K. Vines, K. Nykyri, J. L. Burch, and R. J. Strangeway (2019), Mass loading the earth's dayside magnetopause boundary layer and its effect on magnetic reconnection, *Geophysical Research Letters*, *46*(12), 6204–6213, doi:10.1029/2019GL082384.

Gershman, D. J., A. F-Viñas, J. C. Dorelli, S. A. Boardsen, L. A. Avanov, P. M. Bellan, S. J. Schwartz, B. Lavraud, V. N. Coffey, M. O. Chandler, Y. Saito, W. R. Paterson, S. A. Fuselier, R. E. Ergun, R. J. Strangeway, C. T. Russell, B. L. Giles, C. J. Pollock, R. B. Torbert, and J. L. Burch (2017), Wave-particle energy exchange directly observed in a kinetic Alfvén-branch wave, *Nature Communications*, *8*, 14719, doi:10.1038/ncomms14719.

Graham, D. B., Y. V. Khotyaintsev, C. Norgren, A. Vaivads, M. André, S. Toledo-Redondo, P.-A. Lindqvist, G. T. Marklund, R. E. Ergun, W. R. Paterson, D. J. Gershman, B. L. Giles, C. J. Pollock, J. C. Dorelli, L. A. Avanov, B. Lavraud, Y. Saito, W. Magnes, C. T. Russell, R. J. Strangeway, R. B. Torbert, and J. L. Burch (2017), Lower hybrid waves in the ion diffusion and magnetospheric inflow regions, *Journal of Geophysical Research: Space Physics*, *122*(1), 517–533, doi:10.1002/2016JA023572.

Haaland, S., A. Runov, A. Artemyev, and V. Angelopoulos (2019), Characteristics of the flank magnetopause: Themis observations, *Journal of Geophysical Research: Space Physics*, *124*(5), 3421–3435, doi:10.1029/2019JA026459.

Hasegawa, A. (1976), Particle acceleration by mhd surface wave and formation of aurora, *Journal of Geophysical Research (1896-1977)*, *81*(28), 5083–5090, doi: 10.1029/JA081i028p05083.

Hasegawa, A., and K. Mima (1978), Anomalous transport produced by kinetic alfvén wave turbulence, *Journal of Geophysical Research: Space Physics*, *83*(A3), 1117–1123, doi: 10.1029/JA083iA03p01117.

Hasegawa, H., M. Fujimoto, K. Maezawa, Y. Saito, and T. Mukai (2003), Geotail observations of the dayside outer boundary region: Interplanetary magnetic field control and dawn-dusk asymmetry, *J. Geophys. Res.*, *108(A4)*, doi:10.1029/2002JA009667.

Hasegawa, H., M. Fujimoto, T.-D. Phan, H. Reme, A. Balogh, M. W. Dunlop, C. Hashimoto, and R. TanDokoro (2004), Transport of solar wind into earth's magnetosphere through rolled-up Kelvin-Helmholtz vortices, *Nature*, *430*, 755–758.

Hasegawa, H., M. Fujimoto, K. Takagi, Y. Saito, T. Mukai, and H. Rème (2006), Single-spacecraft detection of rolled-up Kelvin-Helmholtz vortices at the flank magnetopause, *Journal of Geophysical Research (Space Physics)*, *111*, 9203–+, doi: 10.1029/2006JA011728.

Hasegawa, H., A. Retinò, A. Vaivads, Y. Khotyaintsev, M. André, T. K. M. Nakamura, W.-L. Teh, B. U. Ö. Sonnerup, S. J. Schwartz, Y. Seki, M. Fujimoto, Y. Saito, H. Rème, and P. Canu (2009), Kelvin-Helmholtz waves at the Earth's magnetopause: Multiscale development and associated reconnection, *Journal of Geophysical Research (Space Physics)*, *114*, A12207, doi:10.1029/2009JA014042.

Hasegawa, H., T. K. M. Nakamura, D. J. Gershman, Y. Nariyuki, A. F. Viñas, B. L. Giles, B. Lavraud, C. T. Russell, Y. V. Khotyaintsev, R. E. Ergun, and Y. Saito (2020), Generation of turbulence in kelvin-helmholtz vortices at the earth's magnetopause: Magnetospheric multiscale observations, *Journal of Geophysical Research: Space Physics*, *125*(3), e2019JA027,595, doi:10.1029/2019JA027595, e2019JA027595 2019JA027595.

Hellinger, P., P. Trávníček, J. C. Kasper, and A. J. Lazarus (2006), Solar wind proton temperature anisotropy: Linear theory and wind/swe observations, *Geophysical Research Letters*, *33*(9), doi:10.1029/2006GL025925.

Henry, Z. W., K. Nykyri, T. W. Moore, A. P. Dimmock, and X. Ma (2017), On the dawn-dusk asymmetry of the kelvin-helmholtz instability between 2007 and 2013, *Journal of Geophysical Research: Space Physics*, *122*(12), 11,888–11,900, doi: 10.1002/2017JA024548.

Hietala, H., J. F. Drake, T. D. Phan, J. P. Eastwood, and J. P. McFadden (2015), Ion temperature anisotropy across a magnetotail reconnection jet, *Geophysical Research Letters*, *42*(18), 7239–7247, doi:10.1002/2015GL065168.

Hietala, H., T. D. Phan, V. Angelopoulos, M. Oieroset, M. O. Archer, T. Karlsson, and F. Plaschke (2018), In situ observations of a magnetosheath high-speed jet triggering magnetopause reconnection, *Geophysical Research Letters*, *45*(4), 1732–1740, doi: 10.1002/2017GL076525.

Hunana, P., M. L. Goldstein, T. Passot, P. L. Sulem, D. Laveder, and G. P. Zank (2013), POLARIZATION AND COMPRESSIBILITY OF OBLIQUE KINETIC ALFVén WAVES, *The Astrophysical Journal*, *766*(2), 93, doi:10.1088/0004-637x/766/2/93.

Hwang, K.-J., M. L. Goldstein, M. M. Kuznetsova, Y. Wang, A. F. Vikas, and D. G. Sibeck (2012), The first in situ observation of kelvin-helmholtz waves at high-latitude magnetopause during strongly dawnward interplanetary magnetic field conditions, *Journal of Geophysical Research: Space Physics*, *117*(A8), 2156–2202, doi: 10.1029/2011JA017256, a08233.

Hwang, K.-J., K. Dokgo, E. Choi, J. L. Burch, D. G. Sibeck, B. L. Giles, H. Hasegawa, H. S. Fu, Y. Liu, Z. Wang, T. K. M. Nakamura, X. Ma, R. C. Fear, Y. Khotyaintsev, D. B. Graham, Q. Q. Shi, C. P. Escoubet, D. J. Gershman, W. R. Paterson, C. J. Pollock, R. E. Ergun, R. B. Torbert, J. C. Dorelli, L. Avanov, C. T. Russell, and R. J. Strangeway (2020), Magnetic reconnection inside a flux rope induced by kelvin-helmholtz vortices, *Journal of Geophysical Research: Space Physics*, *125*(4), e2019JA027,665, doi:10.1029/2019JA027665, e2019JA027665 2019JA027665.

Johnson, J. R., and C. Z. Cheng (2001), Stochastic ion heating at the magnetopause due to kinetic alfven waves, *Geophys. Res. Lett.*, *28*, 4421–4424.

Johnson, J. R., C. Z. Cheng, and P. Song (1997), Kinetic alfven waves and plasma transport at the magnetopause, *Geophys. Res. Lett.*, *24*, 1423–1426.

Johnson, J. R., C. Z. Cheng, and P. Song (2001), Signatures of mode conversion and kinetic alfven waves at the magnetopause, *Geophys. Res. Lett.*, *28*, 227–230.

Kaminker, V., P. A. Delamere, C. S. Ng, T. Dennis, A. Otto, and X. Ma (2017), Local time dependence of turbulent magnetic fields in saturn's magnetodisc, *Journal of Geophysical Research: Space Physics*, *122*(4), 3972–3984, doi:10.1002/2016JA023834.

Khotyaintsev, Y. V., C. M. Cully, A. Vaivads, M. André, and C. J. Owen (2011), Plasma jet braking: Energy dissipation and nonadiabatic electrons, *Phys. Rev. Lett.*, *106*, 165,001, doi:10.1103/PhysRevLett.106.165001.

King, J. H., and N. E. Papitashvili (2005), Solar wind spatial scales in and comparisons of hourly Wind and ACE plasma and magnetic field data, *Journal of Geophysical Research (Space Physics)*, *110*, A02104, doi:10.1029/2004JA010649.

Lavraud, B., Y. C. Zhang, Y. Vernisse, D. J. Gershman, J. Dorelli, P. A. Cassak, J. Dargent, C. Pollock, B. Giles, N. Aunai, M. Argall, L. Avanov, A. Barrie, J. Burch, M. Chandler, L.-J. Chen, G. Clark, I. Cohen, V. Coffey, J. P. Eastwood, J. Egedal, S. Eriksson, R. Ergun, C. J. Farrugia, S. A. Fuselier, V. Génot, D. Graham, E. Grigorenko, H. Hasegawa, C. Jacquey, I. Kacem, Y. Khotyaintsev, E. MacDonald, W. Magnes, A. Marchaudon, B. Mauk, T. E. Moore, T. Mukai, R. Nakamura, W. Paterson, E. Penou, T. D. Phan, A. Rager, A. Retino, Z. J. Rong, C. T. Russell, Y. Saito, J.-A. Sauvaud, S. J. Schwartz, C. Shen, S. Smith, R. Strangeway, S. Toledo-Redondo, R. Torbert, D. L. Turner, S. Wang, and S. Yokota (2016), Currents and associated electron scattering and bouncing near the diffusion region at earth's magnetopause, *Geophysical Research Letters*, *43*(7), 3042–3050, doi:10.1002/2016GL068359.

Le Contel, O., A. Roux, C. Jacquey, P. Robert, M. Berthomier, T. Chust, B. Grison, V. Angelopoulos, D. Sibeck, C. C. Chaston, C. M. Cully, B. Ergun, K.-H. Glassmeier, U. Auster, J. McFadden, C. Carlson, D. Larson, J. W. Bonnell, S. Mende, C. T. Russell, E. Donovan, I. Mann, and H. Singer (2009), Quasi-parallel whistler mode waves observed by themis during near-earth dipolarizations, *Annales Geophysicae*, *27*(6), 2259–2275, doi:10.5194/angeo-27-2259-2009.

Le Contel, O., P. Leroy, A. Roux, C. Coillot, D. Alison, A. Bouabdellah, L. Mirioni, L. Meslier, A. Galic, M. C. Vassal, R. B. Torbert, J. Needell, D. Rau, I. Dors, R. E. Ergun, J. Westfall, D. Summers, J. Wallace, W. Magnes, A. Valavanoglou, G. Olsson, M. Chutter, J. Macri, S. Myers, S. Turco, J. Nolin, D. Bodet, K. Rowe, M. Tanguy, and B. de la Porte (2016), The Search-Coil Magnetometer for MMS, *Space Science Reviews*, *199*, 257–282, doi:10.1007/s11214-014-0096-9.

Lee, L. C., J. R. Johnson, and Z. W. Ma (1994), Kinetic Alfven waves as a source of plasma transport at the dayside magnetopause, *Journal of Geophysical Research*, *99*, 17,405, doi:10.1029/94JA01095.

Lee, L. C., J. R. Johnson, and Z. W. Ma (1994), Kinetic alfvén waves as a source of plasma transport at the dayside magnetopause, *Journal of Geophysical Research: Space Physics*, *99*(A9), 17,405–17,411, doi:10.1029/94JA01095.

Li, W., J. Raeder, J. Dorelli, M. Oieroset, and T. D. Phan (2005), Plasma sheet formation during long period of northward IMF, *Geophys. Res. Lett.*, *32*, L12S08, doi: 10.1029/2004GL021524.

Li, W., M. André, Y. V. Khotyaintsev, A. Vaivads, D. B. Graham, S. Toledo-Redondo, C. Norgren, P. Henri, C. Wang, B. B. Tang, B. Lavraud, Y. Vernisse, D. L. Turner, J. Burch, R. Torbert, W. Magnes, C. T. Russell, J. B. Blake, B. Mauk, B. Giles, C. Pollock, J. Fennell, A. Jaynes, L. A. Avanov, J. C. Dorelli, D. J. Gershman, W. R. Paterson, Y. Saito, and R. J. Strangeway (2016), Kinetic evidence of magnetic reconnection due to Kelvin-Helmholtz waves, *Geophys. Res. Lett.*, *43*, 5635–5643, doi:

10.1002/2016GL069192.

Lindqvist, P.-A., G. Olsson, R. B. Torbert, B. King, M. Granoff, D. Rau, G. Needell, S. Turco, I. Dors, P. Beckman, J. Macri, C. Frost, J. Salwen, A. Eriksson, L. Åhlén, Y. V. Khotyaintsev, J. Porter, K. Lappalainen, R. E. Ergun, W. Wermeer, and S. Tucker (2016), The Spin-Plane Double Probe Electric Field Instrument for MMS, *Space Science Reviews*, *199*, 137–165, doi:10.1007/s11214-014-0116-9.

Ma, X., and A. Otto (2014), Nonadiabatic heating in magnetic reconnection, *Journal of Geophysical Research: Space Physics*, *119*(7), 5575–5588, doi:10.1002/2014JA019856.

Ma, X., A. Otto, and P. A. Delamere (2014a), Interaction of magnetic reconnection and Kelvin-Helmholtz modes for large magnetic shear: 1. Kelvin-Helmholtz trigger, *Journal of Geophysical Research: Space Physics*, *119*(2), 781–797, doi:10.1002/2013JA019224.

Ma, X., A. Otto, and P. A. Delamere (2014b), Interaction of magnetic reconnection and Kelvin-Helmholtz modes for large magnetic shear: 2. reconnection trigger, *Journal of Geophysical Research: Space Physics*, *119*(2), 808–820, doi:10.1002/2013JA019225.

Ma, X., A. Otto, P. A. Delamere, and H. Zhang (2016), The interaction between reconnection and Kelvin-Helmholtz in the high-latitude magnetopause, *Advances in Space Research*, *58*(2), 231 – 239, doi:http://dx.doi.org/10.1016/j.asr.2016.02.025, Plasma Transport Across Magnetospheric Boundaries.

Ma, X., P. Delamere, A. Otto, and B. Burkholder (2017), Plasma transport driven by the three-dimensional kelvin-helmholtz instability, *Journal of Geophysical Research: Space Physics*, *122*(10), 10,382–10,395, doi:10.1002/2017JA024394.

Ma, X., P. A. Delamere, K. Nykyri, B. Burkholder, B. Neupane, and R. C. Rice (2019), Comparison between fluid simulation with test particles and hybrid simulation for the kelvin-helmholtz instability, *Journal of Geophysical Research: Space Physics*, *124*(8), 6654–6668, doi:10.1029/2019JA026890.

Masson, A., and K. Nykyri (2018), Kelvin–helmholtz instability: Lessons learned and ways forward, *Space Science Reviews*, *214*(4), 71, doi:10.1007/s11214-018-0505-6.

Matsumoto, Y., and M. Hoshino (2004), Onset of turbulence induced by a Kelvin-Helmholtz vortex, *Geophys. Res. Lett.*, *31*, L02807, doi:10.1029/2003GL018195.

Merkin, V. G., J. G. Lyon, and S. G. Claudepierre (2013), Kelvin-Helmholtz instability of the magnetospheric boundary in a three-dimensional global MHD simulation during northward IMF conditions, *Journal of Geophysical Research (Space Physics)*, *118*, 5478–5496, doi:10.1002/jgra.50520.

Miura, A., and P. L. Pritchett (1982), Nonlocal stability analysis of the MHD Kelvin-Helmholtz instability in a compressible plasma, *J. Geophys. Res.*, *87*, 7431–7444, doi: 10.1029/JA087iA09p07431.

Moore, T. W., K. Nykyri, and A. P. Dimmock (2016), Cross-scale energy transport in space plasmas, *Nature Physics*, p. DOI:10.1038/NPHYS3869, doi: DOI:10.1038/NPHYS3869.

Moore, T. W., K. Nykyri, and A. P. Dimmock (2017), Ion-scale wave properties and enhanced ion heating across the low-latitude boundary layer during kelvin-helmholtz instability, *Journal of Geophysical Research: Space Physics*, *122*(11), 11,128–11,153, doi: 10.1002/2017JA024591.

Nakamura, T. K. M., H. Hasegawa, I. Shinohara, and M. Fujimoto (2011), Evolution of an MHD-scale Kelvin-Helmholtz vortex accompanied by magnetic reconnection: Two-dimensional particle simulations, *Journal of Geophysical Research (Space Physics)*, *116*, A03227, doi:10.1029/2010JA016046.

Nykyri, K. (2002), Influence of the Kelvin-Helmholtz instability on the plasma transport at the magnetospheric boundary, Phd thesis, University of Alaska.

Nykyri, K. (2013), Impact of MHD shock physics on magnetosheath asymmetry and Kelvin-Helmholtz instability, *Journal of Geophysical Research (Space Physics)*, *118*, 5068–5081, doi:10.1002/jgra.50499.

Nykyri, K., and A. P. Dimmock (2016), Statistical study of the ULF Pc4-Pc5 range fluctuations in the vicinity of Earth's magnetopause and correlation with the Low

Latitude Boundary Layer thickness, *Advances in Space Research*, *58*, 257–267, doi: 10.1016/j.asr.2015.12.046.

Nykyri, K., and C. Foullon (2013), First magnetic seismology of the CME reconnection outflow layer in the low corona with 2.5-D MHD simulations of the Kelvin-Helmholtz instability, *Geophys. Res. Lett.*, *40*, 4154–4159, doi:10.1002/grl.50807.

Nykyri, K., and A. Otto (2001), Plasma transport at the magnetospheric boundary due to reconnection in Kelvin-Helmholtz vortices, *Geophys. Res. Lett.*, *28*, 3565–3568, doi: 10.1029/2001GL013239.

Nykyri, K., and A. Otto (2004), Influence of the Hall term on KH instability and reconnection inside KH vortices, *Ann. Geophys.*, *22*, 935–949, doi:10.5194/angeo-22-935-2004.

Nykyri, K., A. Otto, B. Lavraud, C. Mouikis, L. Kistler, A. Balogh, and H. Réme (2006), Cluster observations of reconnection due to the Kelvin-Helmholtz instability at the dawn side magnetospheric flank, *Ann. Geophys.*, *24*, 2619–2643.

Nykyri, K., A. Otto, E. Adamson, E. Dougal, and J. Mumme (2011a), Cluster observations of a cusp diamagnetic cavity: Structure, size, and dynamics, *Journal of Geophysical Research (Space Physics)*, *116*, A03228, doi:10.1029/2010JA015897.

Nykyri, K., A. Otto, E. Adamson, and A. Tjulin (2011b), On the origin of fluctuations in the cusp diamagnetic cavity, *Journal of Geophysical Research (Space Physics)*, *116*, A06208, doi:10.1029/2010JA015888.

Nykyri, K., A. Otto, E. Adamson, E. Kronberg, and P. Daly (2012), On the origin of high-energy particles in the cusp diamagnetic cavity, *Journal of Atmospheric and Solar-Terrestrial Physics*, *87*, 70–81, doi:10.1016/j.jastp.2011.08.012.

Nykyri, K., X. Ma, A. Dimmock, C. Foullon, A. Otto, and A. Osmane (2017), Influence of velocity fluctuations on the kelvin-helmholtz instability and its associated mass transport, *Journal of Geophysical Research: Space Physics*, *122*(9), 9489–9512, doi: 10.1002/2017JA024374, 2017JA024374.

Nykyri, K., C. Chu, X. Ma, S. A. Fuselier, and R. Rice (2019a), First MMS observation of energetic particles trapped in high-latitude magnetic field depressions, *Journal of Geophysical Research: Space Physics*, *124*(1), 197–210, doi:10.1029/2018JA026131.

Nykyri, K., M. Bengtson, V. Angelopoulos, Y. Nishimura, and S. Wing (2019b), Can enhanced flux loading by high-speed jets lead to a substorm? multipoint detection of the christmas day substorm onset at 08:17 ut, 2015, *Journal of Geophysical Research: Space Physics*, *124*(6), 4314–4340, doi:10.1029/2018JA026357.

Nykyri, K., X. Ma, and J. Johnson (2020), Cross-scale energy transport in space plasmas: Applications to the magnetopause boundary, *AGU book, The Magnetosphere*, *xx*, accepted.

Otto, A. (1990), 3D resistive MHD computations of magnetospheric physics, *Comput. Phys. Commun.*, *59*, 185–195.

Otto, A., and D. H. Fairfield (2000), Kelvin-Helmholtz instability at the magnetotail boundary: MHD simulation and comparison with Geotail observations, *J. Geophys. Res.*, *105*, 21,175–21,190.

Otto, A., and K. Nykyri (2003), Kelvin-Helmholtz instability and magnetic reconnection: Mass transport at the LLBL, *Washington DC American Geophysical Union Geophysical Monograph Series*, *133*, 53–62, doi:10.1029/133GM05.

Paschmann, G., I. Papamastorakis, N. Sckopke, G. Haerendel, B. U. O. Sonnerup, S. J. Bame, J. R. Asbridge, J. T. Gosling, C. T. Russel, and R. C. Elphic (1979), Plasma acceleration at the earth's magnetopause - Evidence for reconnection, *Nature*, *282*, 243–246, doi:10.1038/282243a0.

Plaschke, F., V. Angelopoulos, and K.-H. Glassmeier (2013), Magnetopause surface waves: Themis observations compared to mhd theory, *Journal of Geophysical Research: Space Physics*, *118*(4), 1483–1499, doi:10.1002/jgra.50147.

Plaschke, F., M. G. G. T. Taylor, and R. Nakamura (2014), Alternative interpretation of results from kelvin-helmholtz vortex identification criteria, *Geophysical Research Letters*, *41*(2), 244–250, doi:10.1002/2013GL058948.

Pollock, C., T. Moore, A. Jacques, J. Burch, U. Gliese, Y. Saito, T. Omoto, L. Avanov, A. Barrie, V. Coffey, J. Dorelli, D. Gershman, B. Giles, T. Rosnack, C. Salo, S. Yokota, M. Adrian, C. Aoustin, C. Auletti, S. Aung, V. Bigio, N. Cao, M. Chandler, D. Chornay, K. Christian, G. Clark, G. Collinson, T. Corris, A. De Los Santos, R. Devlin, T. Diaz, T. Dickerson, C. Dickson, A. Diekmann, F. Diggs, C. Duncan, A. Figueroa-Vinas, C. Firman, M. Freeman, N. Galassi, K. Garcia, G. Goodhart, D. Guererro, J. Hageman, J. Hanley, E. Hemminger, M. Holland, M. Hutchins, T. James, W. Jones, S. Kreisler, J. Kujawski, V. Lavu, J. Lobell, E. LeCompte, A. Lukemire, E. MacDonald, A. Mariano, T. Mukai, K. Narayanan, Q. Nguyan, M. Onizuka, W. Paterson, S. Persyn, B. Piepgrass, F. Cheney, A. Rager, T. Raghuram, A. Ramil, L. Reichenthal, H. Rodriguez, J. Rouzaud, A. Rucker, Y. Saito, M. Samara, J.-A. Sauvaud, D. Schuster, M. Shappirio, K. Shelton, D. Sher, D. Smith, K. Smith, S. Smith, D. Steinfeld, R. Szymkiewicz, K. Tanimoto, J. Taylor, C. Tucker, K. Tull, A. Uhl, J. Vloet, P. Walpole, S. Weidner, D. White, G. Winkert, P.-S. Yeh, and M. Zeuch (2016), Fast Plasma Investigation for Magnetospheric Multiscale, *Space Science Reviews*, *199*, 331–406, doi:10.1007/s11214-016-0245-4.

Russell, C. T., and R. C. Elphic (1978), Initial ISEE magnetometer results: Magnetopause observations, *Space Sci. Rev.*, *22*, 681–715, doi:10.1007/BF00212619.

Russell, C. T., B. J. Anderson, W. Baumjohann, K. R. Bromund, D. Dearborn, D. Fischer, G. Le, H. K. Leinweber, D. Leneman, W. Magnes, J. D. Means, M. B. Moldwin, R. Nakamura, D. Pierce, F. Plaschke, K. M. Rowe, J. A. Slavin, R. J. Strangeway, R. Torbert, C. Hagen, I. Jernej, A. Valavanoglou, and I. Richter (2016), The Magnetospheric Multiscale Magnetometers, *Space Science Reviews*, *199*, 189–256, doi: 10.1007/s11214-014-0057-3.

Sckopke, N., G. Paschmann, G. Haerendel, B. U. O. Sonnerup, S. J. Bame, T. G. Forbes, E. W. Hones Jr., and C. T. Russell (1981), Structure of the low-latitude boundary layer, *Journal of Geophysical Research: Space Physics*, *86*(A4), 2099–2110, doi: 10.1029/JA086iA04p02099.

Song, P., and C. T. Russell (1992), Model for the formation of the low-latitude boundary layer for strongly northward interplanetary magnetic field, *J. Geophys. Res.*, *97*, 1411–1420.

Sonnerup, B. U. O., and L. J. Cahill, Jr. (1967), Magnetopause Structure and Attitude from Explorer 12 Observations, *J. Geophys. Res.*, *72*, 171, doi: 10.1029/JZ072i001p00171.

Sonnerup, B. U. Ö., G. Paschmann, I. Papamastorakis, N. Sckopke, G. Haerendel, S. J. Bame, J. R. Asbridge, J. T. Gosling, and C. T. Russell (1981), Evidence for magnetic reconnection at the earth's magnetopause, *J. Geophys. Res.*, *86*, 10,049–10,067.

Sonnerup, B. U. Ö., G. Paschmann, and T.-D. Phan (1995), Fluid aspects of reconnection at the magnetopause: In situ observations, in *Physics of the Magnetopause,* Geophys. Monogr. Ser., vol. 90, edited by P. Song, B. U. Ö. Sonnerup, and M. F. Thomsen, p. 167, AGU, Washington, D. C.

Sorathia, K. A., V. G. Merkin, A. Y. Ukhorskiy, R. C. Allen, K. Nykyri, and S. Wing (2019), Solar wind ion entry into the magnetosphere during northward imf, *Journal of Geophysical Research: Space Physics*, *124*(7), 5461–5481, doi:10.1029/2019JA026728.

Stawarz, J. E., S. Eriksson, F. D. Wilder, R. E. Ergun, S. J. Schwartz, A. Pouquet, J. L. Burch, B. L. Giles, Y. Khotyaintsev, O. L. Contel, P.-A. Lindqvist, W. Magnes, C. J. Pollock, C. T. Russell, R. J. Strangeway, R. B. Torbert, L. A. Avanov, J. C. Dorelli, J. P. Eastwood, D. J. Gershman, K. A. Goodrich, D. M. Malaspina, G. T. Marklund, L. Mirioni, and A. P. Sturner (2016), Observations of turbulence in a kelvin-helmholtz event on 8 september 2015 by the magnetospheric multiscale mission, *Journal of Geophysical Research: Space Physics*, *121*(11), 11,021–11,034, doi:10.1002/2016JA023458.

Taylor, M. G. G. T., B. Lavraud, C. P. Escoubet, S. E. Milan, K. Nykyri, M. W. Dunlop, J. A. Davies, R. H. W. Friedel, H. Frey, Y. V. Bogdanova, A. Åsnes, H. Laakso,

P. TrávnıČek, A. Masson, H. Opgenoorth, C. Vallat, A. N. Fazakerley, A. D. Lahiff, C. J. Owen, F. Pitout, Z. Pu, C. Shen, Q. G. Zong, H. Rème, J. Scudder, and T. L. Zhang (2008), The plasma sheet and boundary layers under northward IMF: A multi-point and multi-instrument perspective, *Advances in Space Research*, *41*, 1619–1629, doi:10.1016/j.asr.2007.10.013.

Thomas, V. A., and D. Winske (1993), Kinetic simulations of the Kelvin-Helmholtz instability at the magnetopause, *J. Geophys. Res.*, *98*, 11,425–11,438.

Torbert, R. B., C. T. Russell, W. Magnes, R. E. Ergun, P.-A. Lindqvist, O. LeContel, H. Vaith, J. Macri, S. Myers, D. Rau, J. Needell, B. King, M. Granoff, M. Chutter, I. Dors, G. Olsson, Y. V. Khotyaintsev, A. Eriksson, C. A. Kletzing, S. Bounds, B. Anderson, W. Baumjohann, M. Steller, K. Bromund, G. Le, R. Nakamura, R. J. Strangeway, H. K. Leinweber, S. Tucker, J. Westfall, D. Fischer, F. Plaschke, J. Porter, and K. Lappalainen (2016), The FIELDS Instrument Suite on MMS: Scientific Objectives, Measurements, and Data Products, *Space Science Reviews*, *199*, 105–135, doi:10.1007/s11214-014-0109-8.

Tsyganenko, N. A. (1996), Effects of the solar wind conditions on the global magnetospheric configuration as deduced from data-based field models, in *Proceedings of the ICS-3 Conference on substorms (Versailles, France May 12-17, 1996)*, pp. 181–185, ESA SP-389.

Vetoulis, G., and J. F. Drake (1999), Whistler turbulence at the magnetopause 1. Reduced equations and linear theory, *J. Geophys. Res.*, *104*, 6919–6928, doi:10.1029/1998JA900112.

Vines, S. K., S. A. Fuselier, S. M. Petrinec, K. J. Trattner, and R. C. Allen (2017), Occurrence frequency and location of magnetic islands at the dayside magnetopause, *Journal of Geophysical Research: Space Physics*, *122*(4), 4138–4155, doi:10.1002/2016JA023524.

Walsh, A. P., S. Haaland, C. Forsyth, A. M. Keesee, J. Kissinger, K. Li, A. Runov, J. Soucek, B. M. Walsh, S. Wing, and M. G. G. T. Taylor (2014), Dawnâ€“dusk asymmetries in the coupled solar windâ€“magnetosphereâ€“ionosphere system: a review, *Annales Geophysicae*, *32*(7), 705–737, doi:10.5194/angeo-32-705-2014.

Wang, C.-P., M. Gkioulidou, L. R. Lyons, and V. Angelopoulos (2012), Spatial distributions of the ion to electron temperature ratio in the magnetosheath and plasma sheet, *Journal of Geophysical Research (Space Physics)*, *117*, 8215, doi:10.1029/2012JA017658.

Wilber, M., and R. M. Winglee (1995), Dawn-dusk asymmetries in the low-latitude boundary layer arising from the Kelvin-Helmholtz instability: A particle simulation, *J. Geophys. Res.*, *100*, 1883–1898.

Wilder, F. D., R. E. Ergun, S. J. Schwartz, D. L. Newman, S. Eriksson, J. E. Stawarz, M. V. Goldman, K. A. Goodrich, D. J. Gershman, D. M. Malaspina, J. C. Holmes, A. P. Sturner, J. L. Burch, R. B. Torbert, P.-A. Lindqvist, G. T. Marklund, Y. Khotyaintsev, R. J. Strangeway, C. T. Russell, C. J. Pollock, B. L. Giles, J. C. Dorrelli, L. A. Avanov, W. R. Patterson, F. Plaschke, and W. Magnes (2016), Observations of large-amplitude, parallel, electrostatic waves associated with the kelvin-helmholtz instability by the magnetospheric multiscale mission, *Geophysical Research Letters*, *43*(17), 8859–8866, doi:10.1002/2016GL070404.

Wing, S., J. R. Johnson, J. Jen, C.-I. Meng, D. G. Sibeck, K. Bechtold, J. Freeman, K. Costello, M. Balikhin, and K. Takahashi (2005), Kp forecast models, *Journal of Geophysical Research: Space Physics*, *110*(A4), doi:10.1029/2004JA010500.

Wing, S., J. R. Johnson, C. C. Chaston, M. Echim, C. P. Escoubet, B. Lavraud, C. Lemon, K. Nykyri, A. Otto, J. Raeder, and C.-P. Wang (2014), Review of Solar Wind Entry into and Transport Within the Plasma Sheet, *Space Science Reviews*, *184*, 33–86, doi:10.1007/s11214-014-0108-9.

Young, D. T., J. L. Burch, R. G. Gomez, A. De Los Santos, G. P. Miller, P. Wilson, N. Paschalidis, S. A. Fuselier, K. Pickens, E. Hertzberg, C. J. Pollock, J. Scherrer, P. B.

Wood, E. T. Donald, D. Aaron, J. Furman, D. George, R. S. Gurnee, R. S. Hourani, A. Jacques, T. Johnson, T. Orr, K. S. Pan, S. Persyn, S. Pope, J. Roberts, M. R. Stokes, K. J. Trattner, and J. M. Webster (2016), Hot plasma composition analyzer for the magnetospheric multiscale mission, *Space Science Reviews*, *199*(1), 407–470, doi: 10.1007/s11214-014-0119-6.

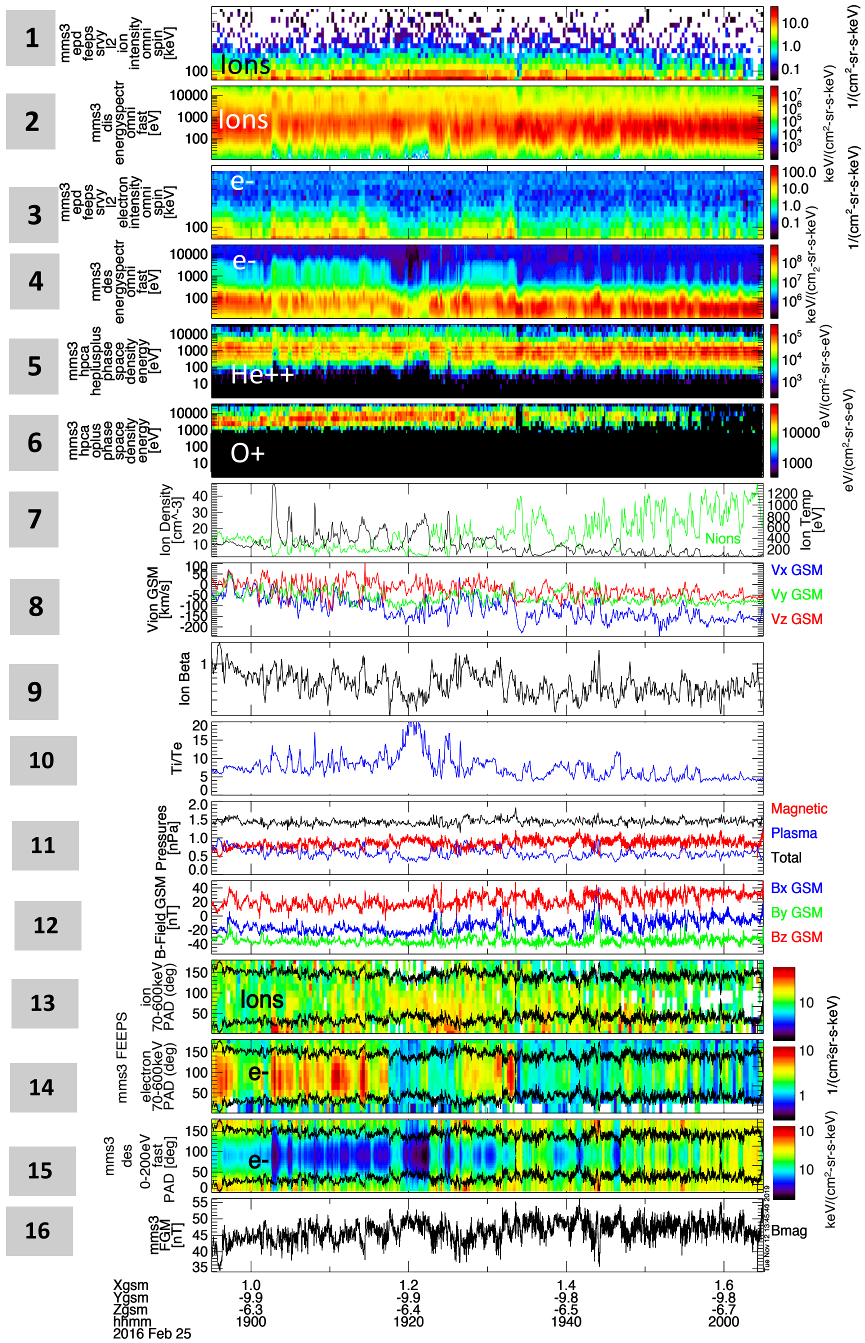

Figure 2. Overview plot of the MMS 3 observations between 18:55-20:05 UT on 25th of February 2016. Panels from top to bottom show energetic ions from FEEPS instrument (1); low energy ions from FPI instrument (2); energetic electrons from the FEEPS instrument (3); low energy electrons from FPI instrument (4); He^{++} (5) and O^{+} (6) from the HPCA instrument. Next three panels use ion and electron moments from the FPI instrument showing the Ion temperature (black line) and density (green line) (7); ion velocity (8); ion plasma beta (9), Ion to electron temperature ratio, T_i/T_e (10). Following panels present total, magnetic and plasma pressure (11), magnetic field (12); 70-600 keV ion (13) and electron (14) spin averaged pitch angle distributions from the FEEPS instrument together with the loss cone (black line), computed in a similar way as in [*Nykyri et al.*, 2019a]; fast mode FPl low energy electron pitch angle distributions (15) and magnetic field strength (16). The plot uses the survey mode FEEPS and FGM data, and the fast mode FPI data.

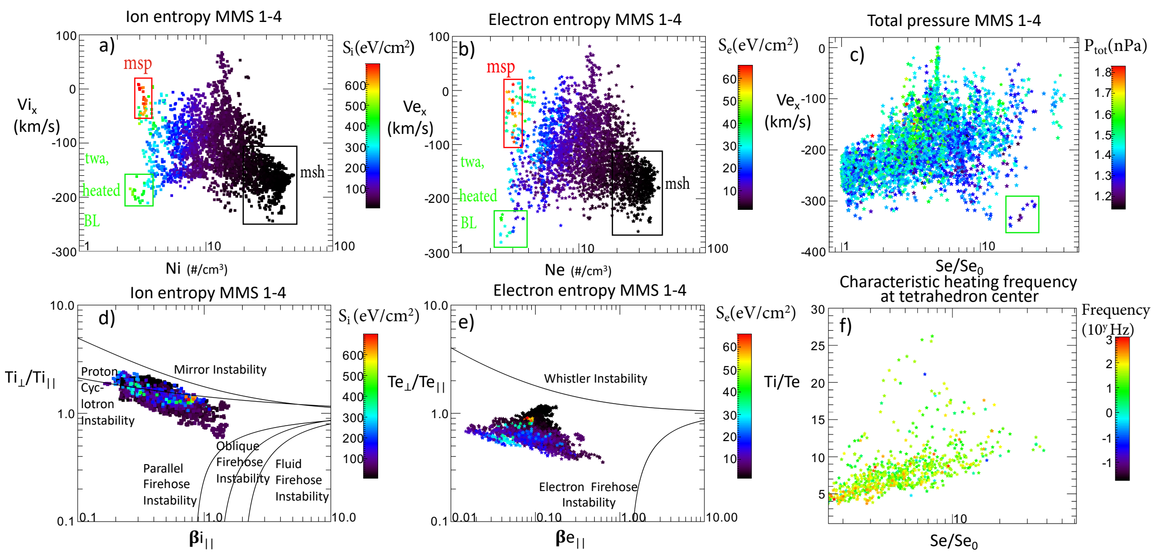

Figure 3. Scatter plots of the v_x component of the ion (a) and electron (b) velocities vs ion and electron densities for MMS 1-4. The color scale is the ion and and electron specific entropy, respectively. Electron velocity vs normalized electron entropy for MMS 1-4. The color code is the total plasma pressure (c). Ion $T_{\|}/T_{\perp}$ vs parallel ion beta for MMS 1-4 (d). Color code is the ion entropy. The lines show ion cyclotron and mirror mode instability curves, and the curves for parallel, oblique and fluid firehose instability. Same for electron plasma moments are shown in panel e). The solid lines present electron whistler and electron firehose instabilities. Ion to electron temperature ratio vs normalized electron entropy (f). The color code is the characteristic heating rate. Data points in panels a-e (f) are sorted with increasing entropies (heating rate) so that the points corresponding to the highest entropy (highest heating rate) are plotted last. The plots are using fast mode FPI data and the electric field and FGM magnetic field data are downsampled to the FPI time cadence. The green, red and black rectangles show the i) tail-ward-accelerated (twa) and heated, ii) magnetospheric, iii) magnetosheath-like plasma populations, respectively.

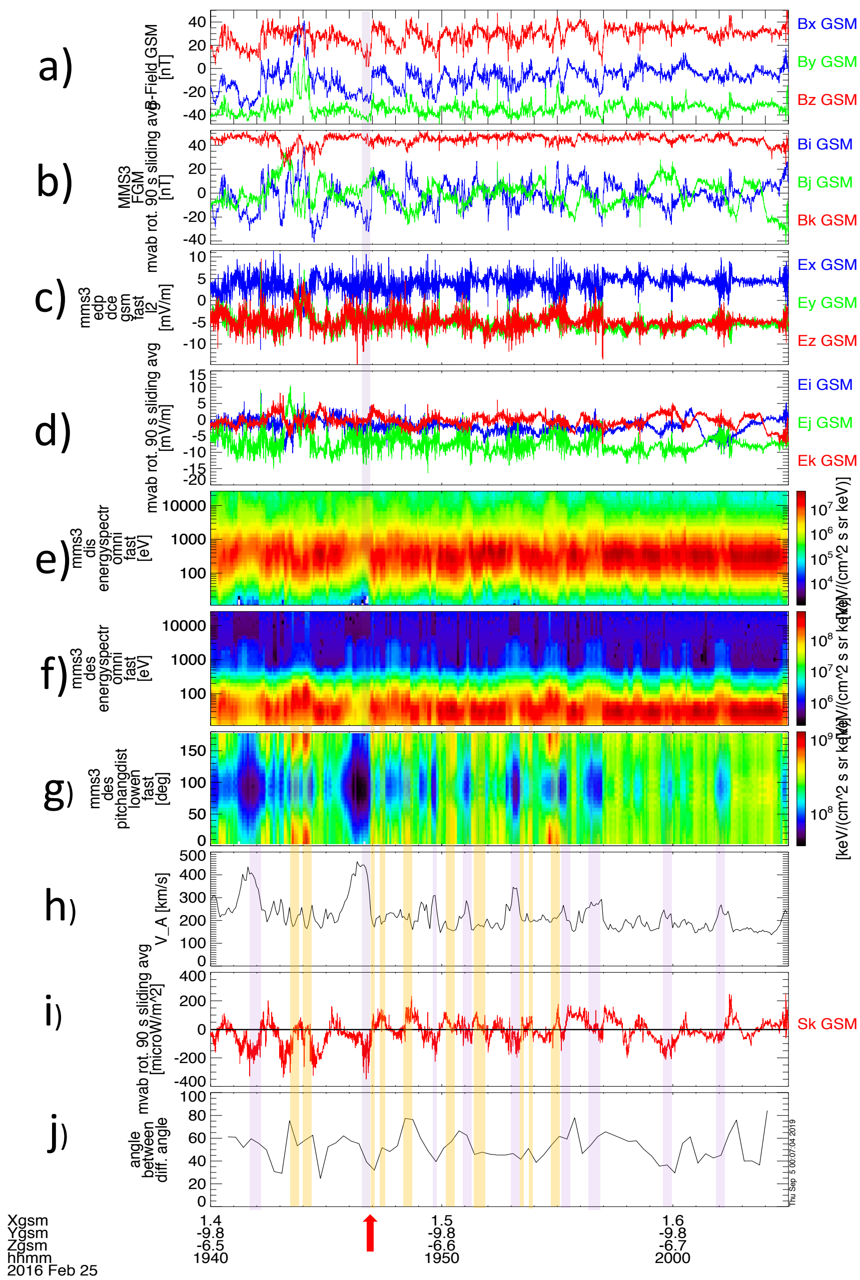

Figure 4. MMS 3 observations between 19:40-20:05 UT. Panels from top to bottom present magnetic field (a), magnetic field rotated into 90 s sliding window MVAB boundary normal coordinates (b), electric field (c), electric field rotated into boundary normal coordinates (d), low energy ion (e) and electron (f) spectrograms, low energy electron pitch angle distribution (g), Alfvén speed (h), and the Poynting flux (using EDP and FGM data) rotated along the 90 s sliding window minimum variance direction (i), and angle between 90 s minimum variance direction and average boundary normal direction (j). The positive peaks of the Poynting flux, enhanced fluxes of counter-streaming electrons are depicted with orange columns whereas the troughs in the Poynting flux are depicted with purple columns. Red arrow show the interval that is studied in detail using multi-spacecraft methods.

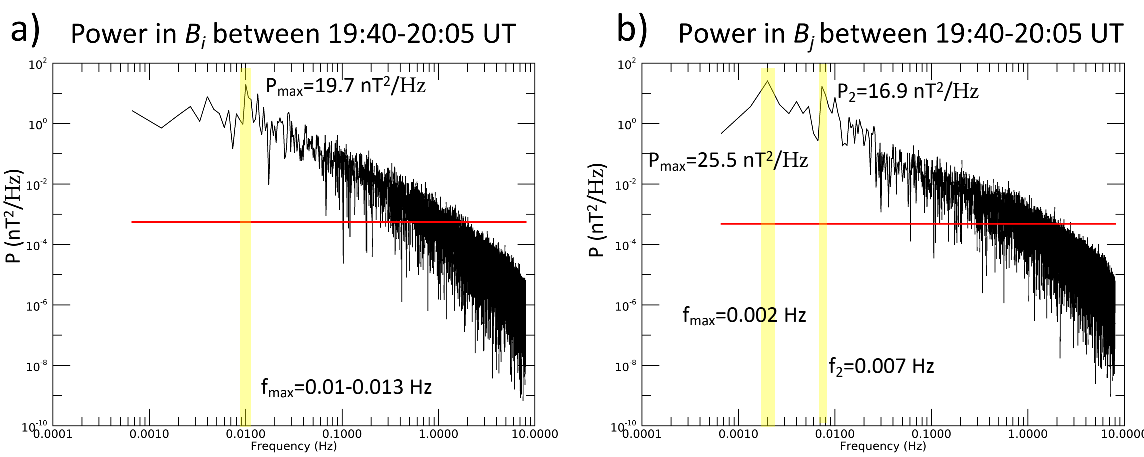

448 **Figure 5.** Power spectra of the B_i (a) and B_j (b) fluctuation power as measured by MMS 3 between 19:40-
449 20:05 UT. The time series of B_i and B_j are shown in Figure 4b. The highlighted columns show the peak
450 frequencies and corresponding powers.

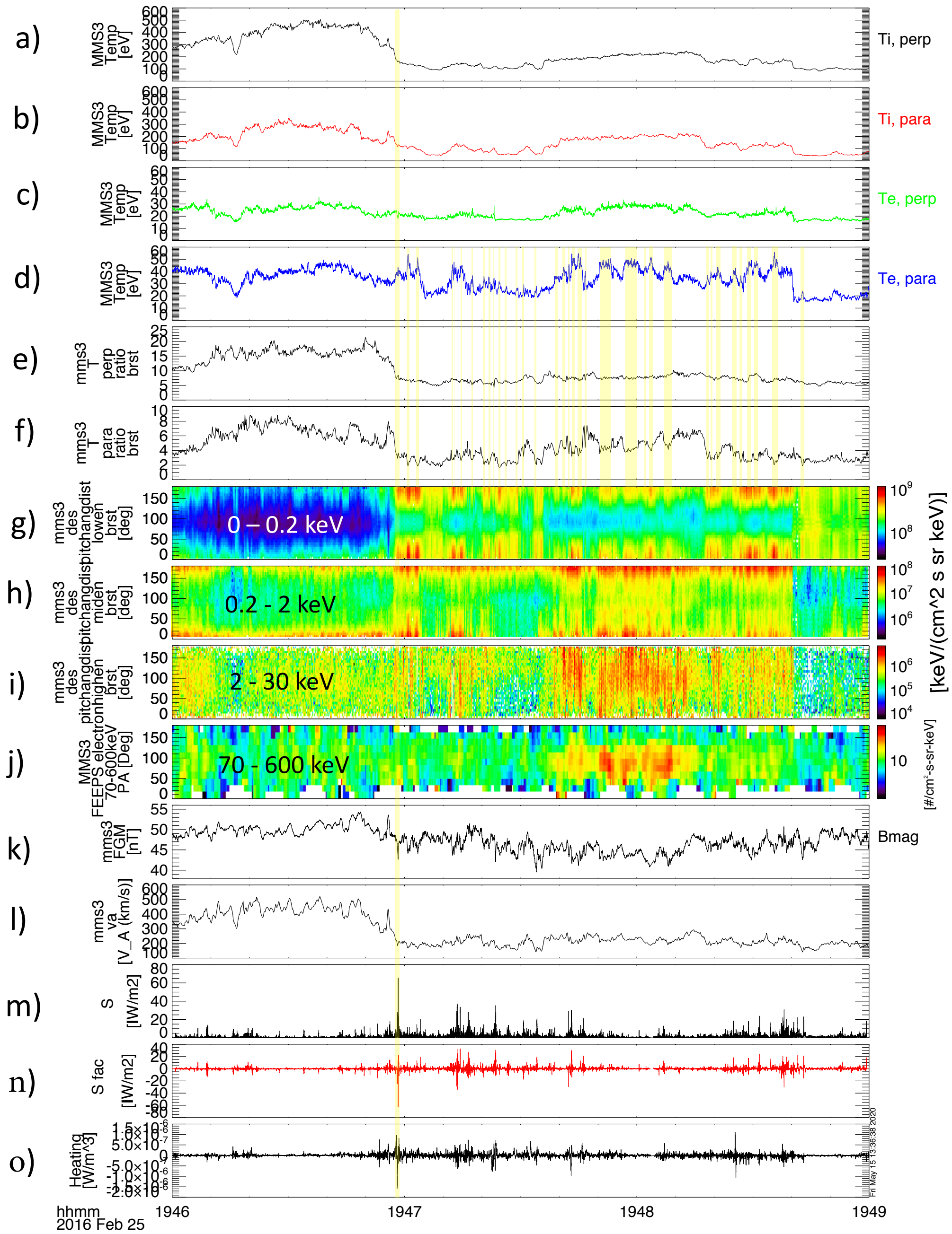

Figure 6. Ion (panels a and b) and electron (panels c and d) perpendicular and parallel temperatures, respectively. Ion to electron perpendicular (panel e) and parallel (panel f) temperature ratio. 0-200 eV (g), 200 eV-2 keV (h), 2 keV-30 keV (i) anf 70-600 kev (j) electron pitch angle distributions from FPI (g-i) and FEEPS (j), respectively. Magnetic field strength (k) and local Alfvén speed (l). Total (m) and the field aligned (n) Poynting flux computed from E and B-field wave forms filtered between 1-4096 Hz. Anomalous Ohmic heating, $J \cdot (E + V_e \times B)$ (o). The plot is created using burst mode data.

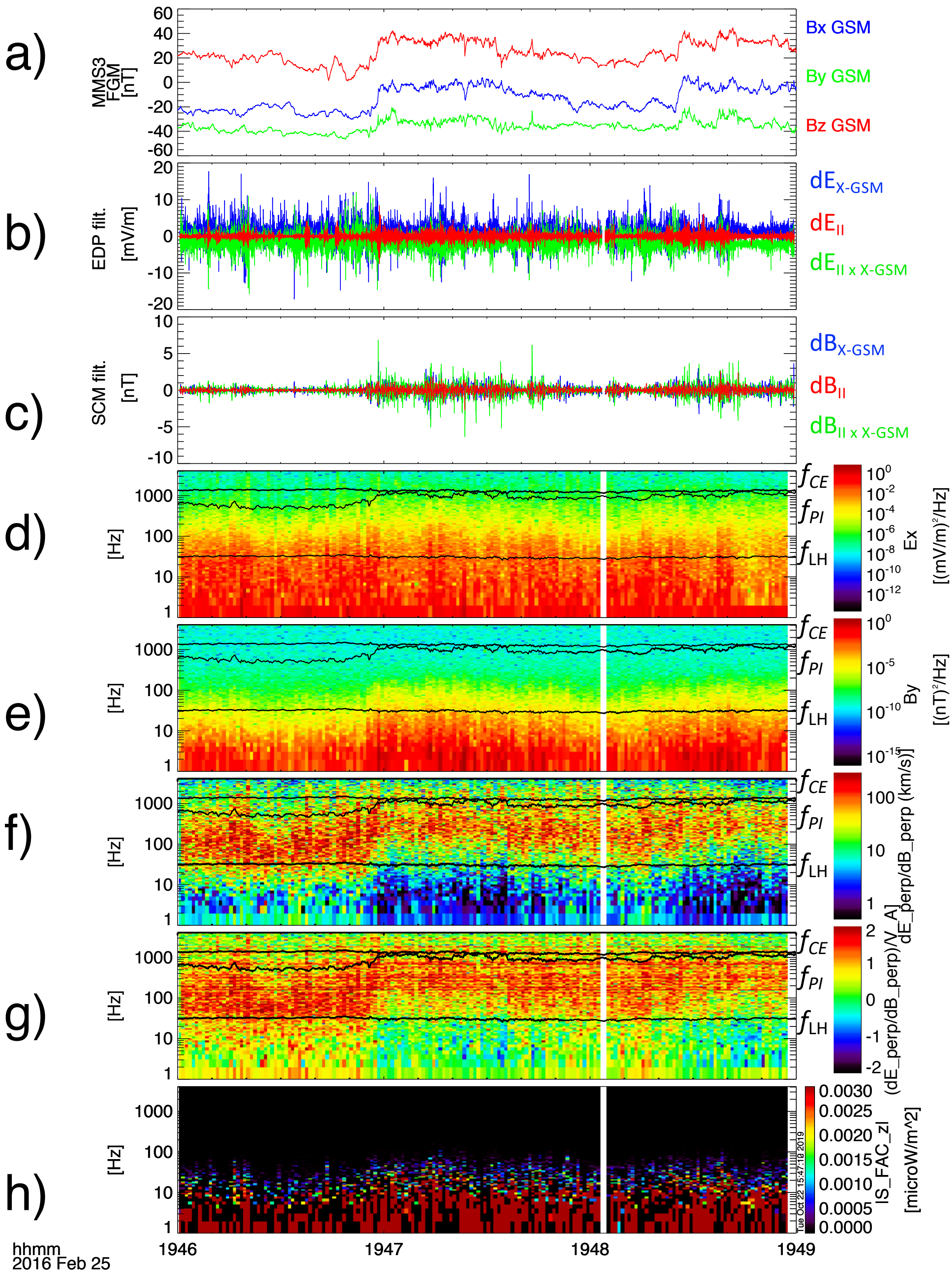

599 **Figure 7.** MMS 3 wave analysis for 19:46:00-19:49:00. Panels a-c show background magnetic field (from
600 FGM), electric field, and high frequency magnetic field (from SCM). Panels d-h present spectrogram of
601 E_x, B_y, $dE_\perp/dB_\perp$, Alfvén speed normalized $dE_\perp/dB_\perp$, and the spectrogram of the field-aligned Poynting
602 flux. The AC electric and magnetic field components are shown in the field-aligned coordinate system where
603 the red color corresponds to component along the magnetic field, blue is the GSM (and GSE) x-axis, and
604 the green component is computed from the cross-product and completes the coordinate system. The plot is
605 created using burst mode data.

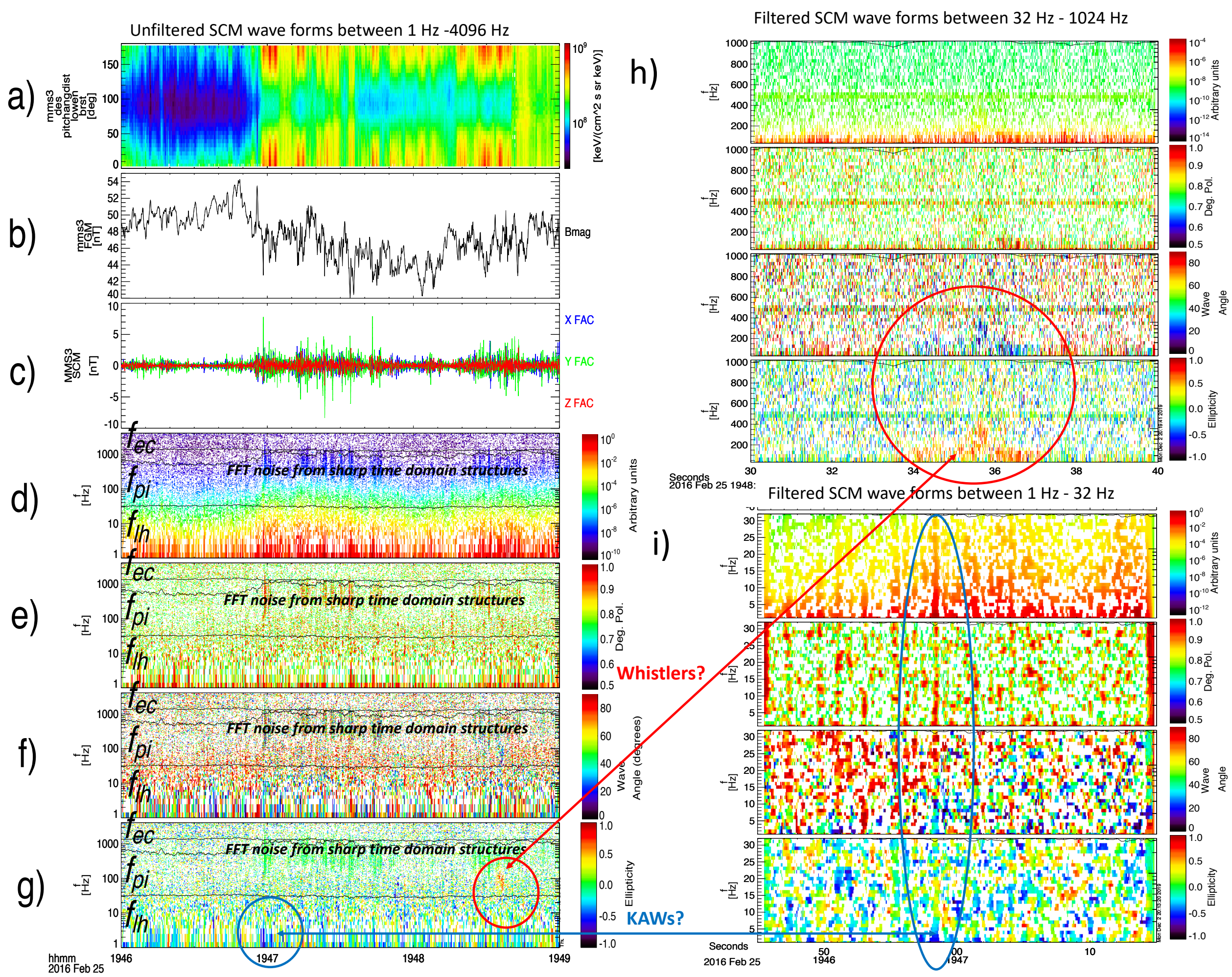

606 **Figure 8.** MMS 3 wave analysis for 19:46:00-19:49:00. Panels a-c show electron pitch angle distributions,
607 background magnetic field strength, and high frequency magnetic field. Panels d-g present various wave
608 properties in spacecraft frame showing wave power spectrogram, degree of polarization for waves, wave prop-
609 agation angle, and ellipticity for the unfiltered SCM waveforms between 1-4096 Hz. Plots h) and i) show the
610 same bottom 4 panels as in panels c-g, except for zoomed intervals for the filtered wave forms between 32-
611 1024 Hz (h) and 1-32 Hz (i) between 19:48:30-19:48:40 UT (h) and 19:46:45-19:47:15 UT (i), respectively.
612 Wave properties are only shown for the well polarized wave intervals for which polarization > 0.7. The plot is
613 created using SCM burst mode (8192 Hz sampling rate) data.

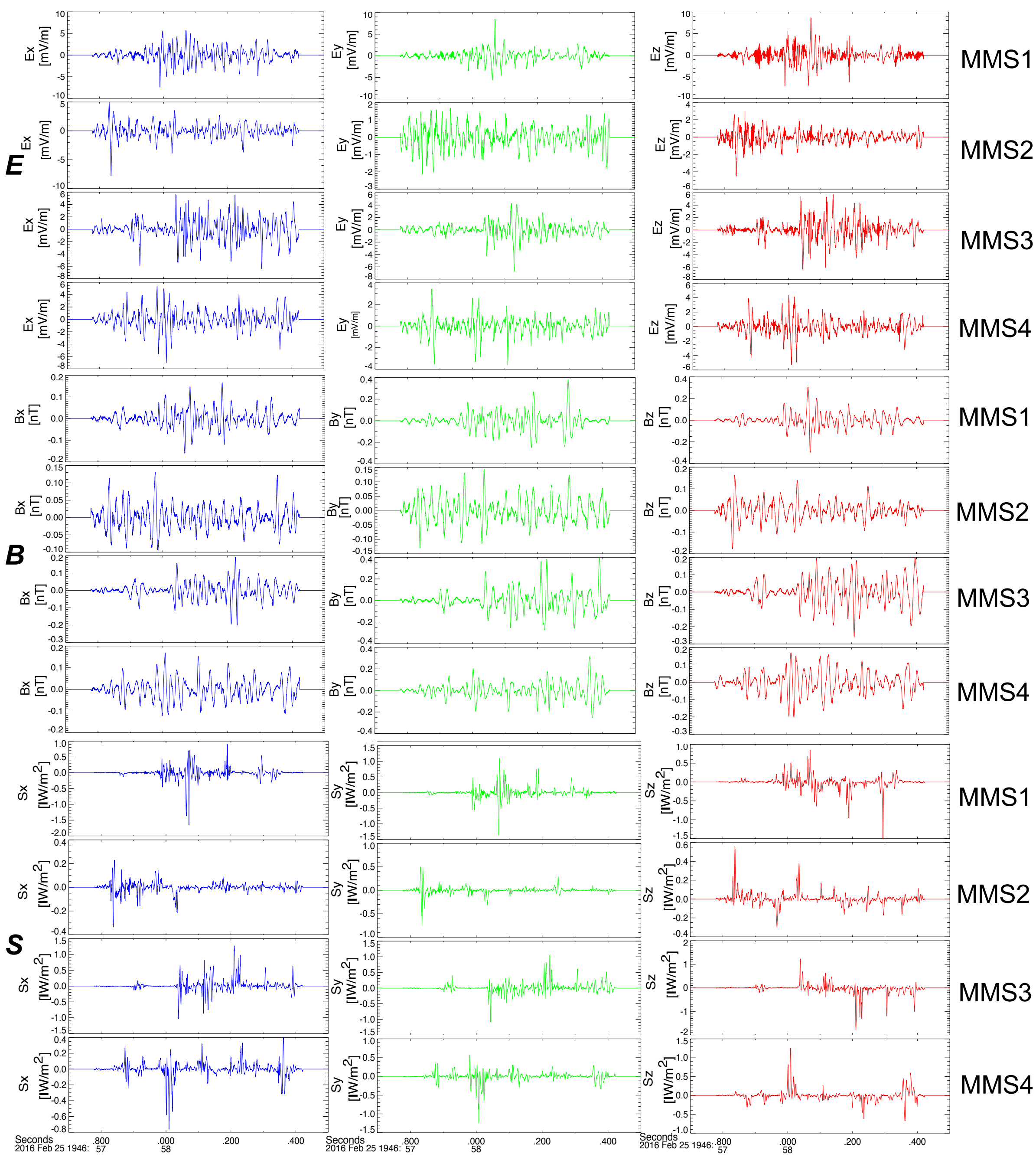

Figure 9. Electric and magnetic field wave form components in GSE coordinates for 0.8 second interval starting at 19:46:57.7 between 32 Hz to 4096 Hz and corresponding components of the wave Poynting flux. The plot is created using burst mode data.

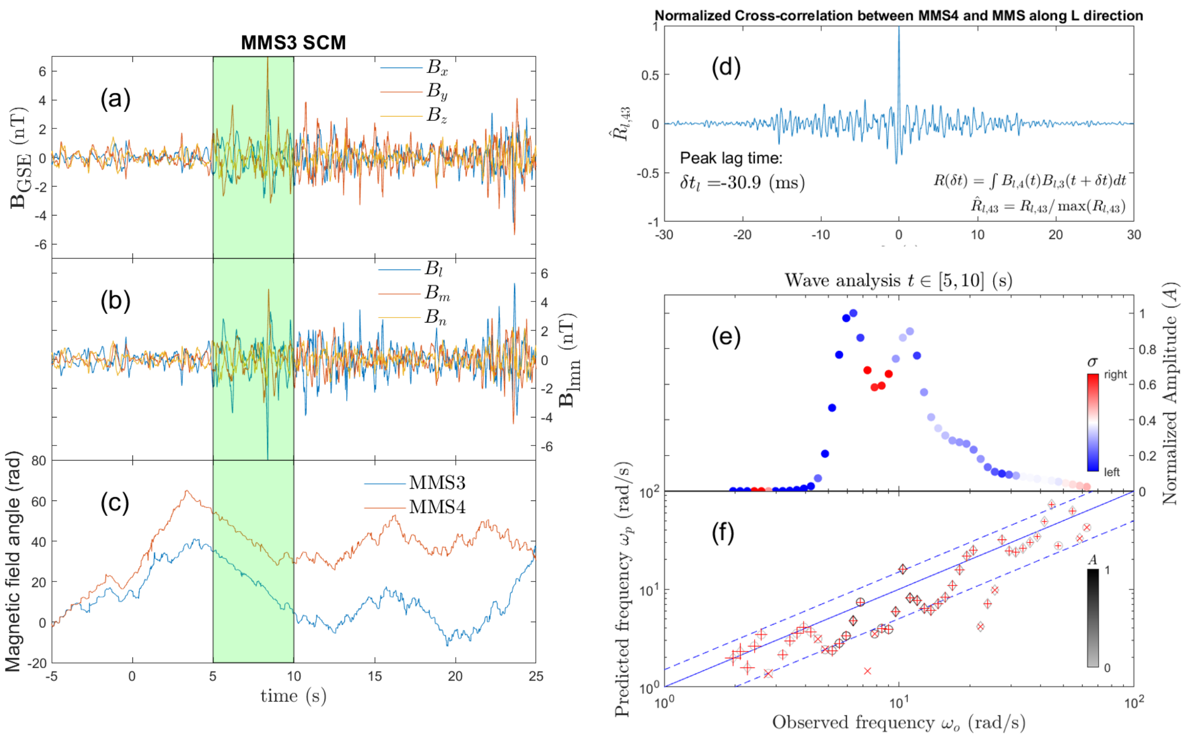

Figure 10. MMS 3 and 4 wave analysis for 19:46:45-19:47:15. Panels show MMS 3 magnetic field in GSE (a) and LMN (b) coordinates, angle between magnetic field $B_{L,M}$ components for MMS 3 and 4 (c), normalized cross-correlation of magnetic field B_L components from MMS3 and MMS4 (d), wave amplitude $\int A(\omega_0, t)dt$ as a function of the observed frequency, ω_o (e), predicted wave frequency with doppler shift vs the observed wave frequency (f), The solid blue line indicates when the predicted value is equal to the observation, and the two dashed blue lines represent 50% deviation.

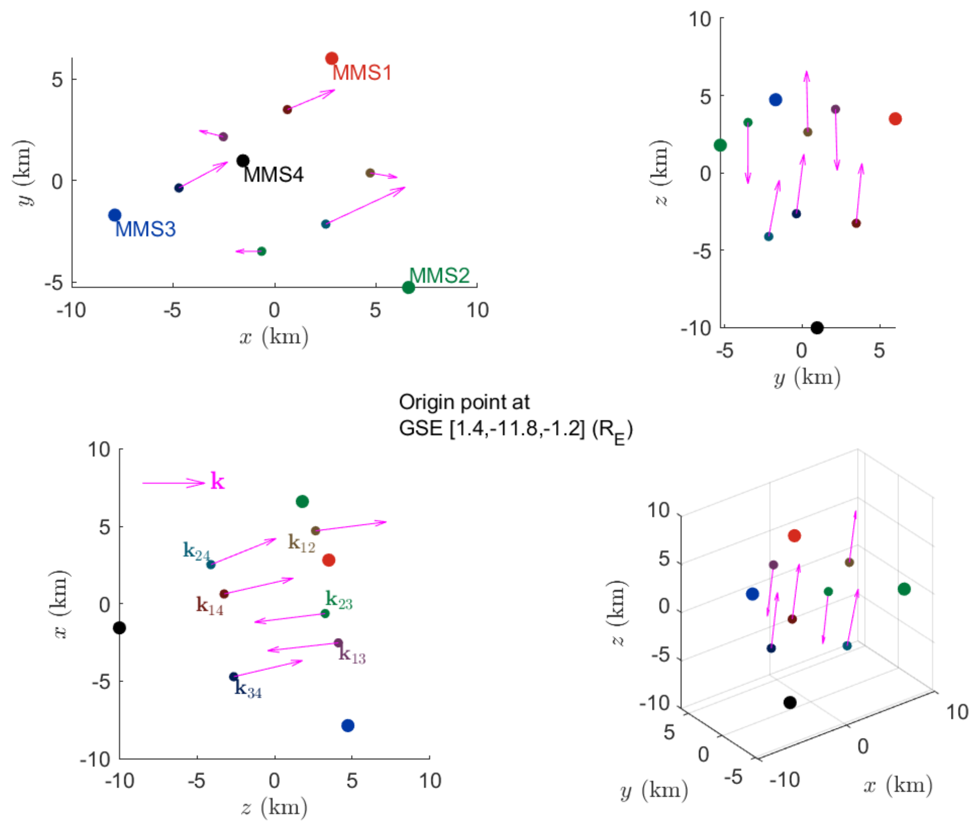

Figure 11. The big dots represent the location of the four MMS spacecraft in red (1), green (2), blue (3), and black (4), respectively during the wave k-vector determination at 19:46:45-19:47:15. The arrows indicate the direction of the wave vectors corresponding to the largest wavelet amplitudes for each pair of spacecraft, which are labeled in the middle of each pair of spacecraft.

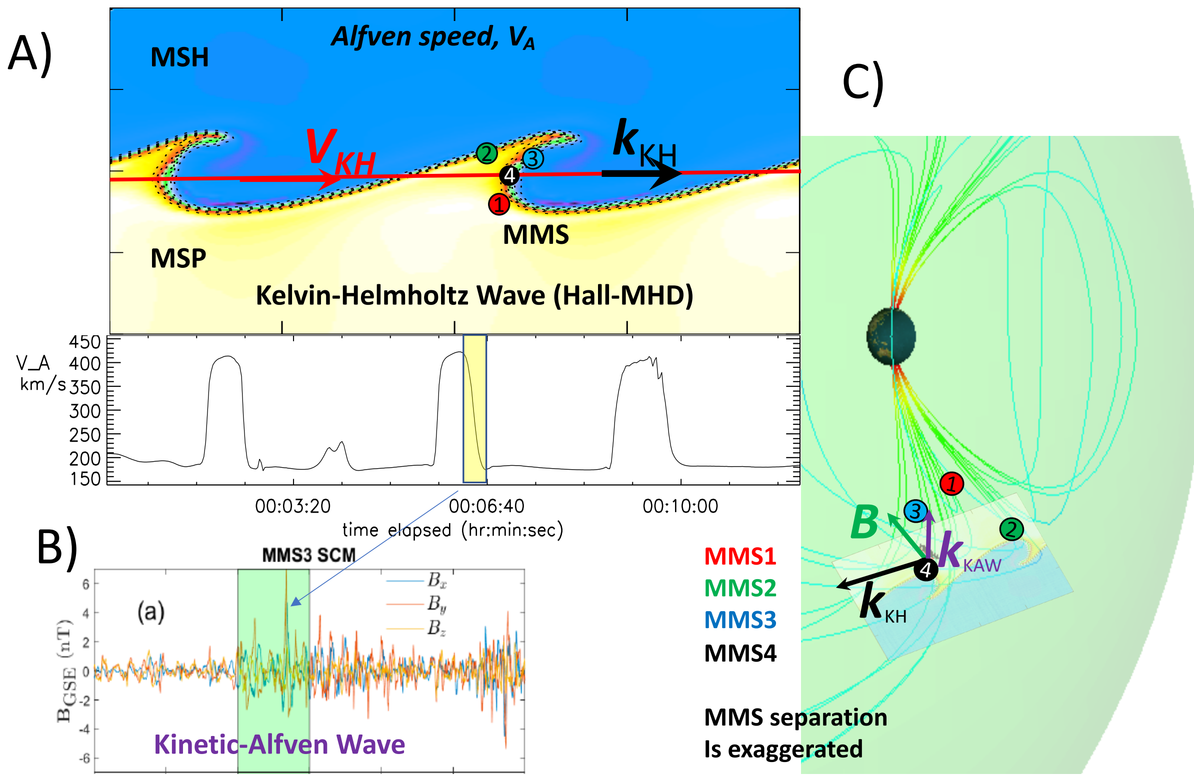

Figure 12. Schematic of the large-scale boundary structure by using a 2-D Hall-MHD simulation [*Nykyri and Otto*, 2004] (see Supplementary Information) showing fluid-scale (λ_{KH} =4.4 R_E) Kelvin-Helmholtz waves (panel a) and observation location of the KAWs with λ_{KAW} $\approx$ 200 km. The background color shows the Alfvén speed which is larger on the magnetospheric (yellow) than on the magnetosheath (blue) side. Virtual probe time-series measurements of the Alfvén speed during the simulation are shown with black trace. MMS observed strong kinetic-scale wave activity (panel b), with the largest amplitude waves identified as kinetic Alfvén waves (KAWs) at the Alfvén velocity gradient. Waves were identified by constructing an experimental dispersion relation using a two-spacecraft method [*Balikhin et al.*, 1997; *Dimmock et al.*, 2013; *Moore et al.*, 2016]. Panel c shows the schematic of the KH wave propagation direction, KAW propagation direction and background magnetic field orientation superposed on Tsyganenko 96 magnetic field model. The various propagation angles are described in the text.